

Discovery of Cycle-to-cycle Modulated Spectral Line Variability and Velocity Gradients in Long-period Cepheids [★]

Richard I. Anderson^{1,2,3†}

¹Physics and Astronomy Department, The Johns Hopkins University, 3400 North Charles St, Baltimore, MD 21202, USA

²Swiss National Science Foundation Fellow

³Département d'Astronomie, Université de Genève, 51 Ch. des Maillettes, CH-1290 Sauverny, Switzerland

19 August 2016

ABSTRACT

This work reports the discovery of cycle-to-cycle modulated spectral line and atmospheric velocity gradient variability in long-period Cepheids based on 925 high-resolution optical spectra of ℓ Carinae ($P \sim 35.5$ d) recorded during three heavy duty-cycle monitoring campaigns (in 2014, 2015, and 2016). Spectral line variability is investigated via cross-correlation functions (CCFs) computed using three sets of spectral lines (weak, solar, strong). A metallic line velocity gradient, $\delta v_r(t)$, is computed as the difference between weak and strong-line RVs. CCF shape indicators BIS (asymmetry), FWHM, and depth all exhibit clear phase-dependent variability patterns that differ from one pulsation cycle to the next. Weak-line CCFs exhibit these effects more clearly than strong-line CCFs. BIS exhibits the most peculiar modulated variability and can be used to identify the presence of cycle-to-cycle modulated line profile variations. $\delta v_r(t)$ clearly exhibits cycle-to-cycle differences that correlate very closely with modulated BIS variability, suggesting perturbations of the atmospheric velocity field as the cause for modulated spectral line variability. These perturbations are most significant during contraction and are not in phase with the pulsation, transmitting information between consecutive pulsation cycles. This work shows RV curve modulation to be a consequence of atmospheric velocity gradient perturbations. Possible origins of these perturbations and their impact on Cepheid RV measurements as well as the projection factor used in Baade-Wesselink-type distance determinations are discussed.

Key words: line: profiles – techniques: radial velocities – stars: individual: ℓ Carinae = HD 84810 = HIP 47854 – stars: variables: Cepheids – stars: oscillations – distance scale

1 INTRODUCTION

Classical Cepheid variable stars (henceforth: Cepheids) are of great interest for several astrophysical and cosmological applications. This includes calibrating the extragalactic distance scale with unprecedented accuracy (Riess et al. 2016) and serving as high-sensitivity test beds for state-of-the-art stellar evolution models (e.g. Anderson et al. 2016b). Cepheids provide crucial insights into stellar structure and oscillations thanks to their high-amplitude radial oscillations that can be studied photometrically (Goodricke 1786), spectroscopically (Belopolsky 1894), and interferometrically (Nordgren et al. 2000; Kervella et al. 2001). The long-period Cepheid ℓ Carinae is a particularly interesting specimen, since its variability can be resolved with great precision using all three meth-

ods thanks to its brightness and large angular diameter (Anderson et al. 2016a, henceforth: A16).

Cepheid variability is frequently thought to be well-understood and relatively simple. While this is true in comparison with other types of stellar variability, recent advances in instrumentation are revealing exciting new features of Cepheid pulsations. Of particular relevance for this work is *modulated variability*, i.e., irregularities of the variability that can occur between consecutive pulsation cycles—referred to here as cycle-to-cycle modulation—as well as on longer timescales (months to years).

Modulated variability was discovered in the sole classical Cepheid located inside the original *Kepler* field, V1154 Cygni, whose pulsation period and amplitude vary rapidly (Derekas et al. 2012). Two further Cepheids observed with space-based high-quality photometry—via the *MOST* satellite—were also shown to exhibit cycle-to-cycle changes (Evans et al. 2015b). However, detecting such variability is not straightforward, even with photometry from space (Poretti et al. 2015). Longer temporal baselines, albeit with lower photometric precision, are achievable from the

[★] Based on observations collected using the CORALIE echelle spectrograph mounted to the Swiss 1.2m Euler telescope located at ESO La Silla Observatory, Chile.

[†] E-mail: ria@jhu.edu

ground, and data from the *Optical Gravitational Lensing Experiment (OGLE)* have been used to identify peculiarities in the light curves and frequency spectra of hundreds of Cepheids (Soszyński et al. 2008, 2015a,b), the majority of which are short-period Cepheids pulsating in the first overtone.

These new indications of additional complexity in Cepheid pulsations have to be considered in the context of similar results obtained for other types of pulsating stars, such as δ Sct and γ Dor stars (e.g. Bowman et al. 2016; Guzik et al. 2016). Additionally, the well-known Blažko (1907) effect among RR Lyrae stars has been studied in exquisite detail using *Kepler* photometry (Kolenberg et al. 2010; Szabó et al. 2010).

Recently, Anderson (2014, henceforth: A14) reported the discovery of modulated radial velocity (RV) variability of four Cepheids, two of which—QZ Nor and V335 Pup—are short-period Cepheids likely to pulsate in the first overtone and candidates for Blažko-effect-like long-timescale modulations (years) similar to the enigmatic V473 Lyr (Burki et al. 1982; Molnár et al. 2013). The two additional Cepheids presented in A14— ℓ Car and RS Pup—are long-period Cepheids for which significant RV curve modulations among consecutive pulsation cycles were detected, varying in particular the RV amplitude. For ℓ Car, this effect was further investigated in a campaign combining contemporaneous spectroscopy and long-baseline near infrared (NIR) interferometry (A16).

Modulated RV variability represents a significant difficulty for at least two types of studies involving Cepheids. Firstly, the change in RV amplitude translates into time-dependent RV curve integrals, which represent a systematic uncertainty for Baade (1926)–Wesselink (1946) (BW) distance determination (A14). Additionally, projection factors required by BW methods appear to be subject to a complex time (cycle-to-cycle) dependence, since modulation affects RV variability and angular diameter variations differently (A16). Secondly, RV curve modulation acts as noise for the detection of low-mass companions to Cepheids, at times leading to apparent time variations in the pulsation-averaged velocity v_γ . This complicates the interpretation of time variable v_γ on the order of a few hundred m s^{-1} and impacts the determination of upper limits for non-binary Cepheids (cf. Evans et al. 2015a, and R. I. Anderson et al. submitted).

The origin of modulated variability in Cepheids is currently largely unclear, although different mechanisms that have been suggested may be related, such as strange-mode and non-radial pulsations, magnetic cycles, or granulation (Buchler et al. 1997; Buchler & Kolláth 2001; Kovtyukh et al. 2003; Stothers 2009; Neilson & Ignace 2014). As mentioned in A14, the very different timescale of RV curve modulation found in long and short-period Cepheids suggests that multiple mechanisms may be at play. Additionally, the link between RV curve modulation and photometric period and amplitude variations remains as yet to be established. High-precision photometric observations of ℓ Car using the *BRITe* satellites could close this important gap.

This paper aims at providing new insights into the origin of such complex cycle-to-cycle modulations by investigating spectral line shape variability. As a first step towards a more detailed description based on individual lines, it focuses on cross-correlation functions (CCFs) computed for 925 high-quality, high-resolution optical spectroscopic data of ℓ Car. This is appropriate, since CCFs are used to infer high-precision RVs among which RV curve modulation was discovered. CCFs have the further benefit of greatly enhanced signal-to-noise ratios (SNR) compared to individual spectral lines and are thus well-suited to search even for weak signs of modulated variability.

The structure of the paper is as follows. Section 2 describes the observational data and presents the quantities investigated in the following sections, including proxies for CCF asymmetry as well as RVs computed at different atmospheric levels and the impact of different RV measurement methods. Section 3 presents a comprehensive overview of ℓ Car’s modulated spectroscopic variability, starting with RVs based on different measurement definitions in §3.1.2. §3.2 then illustrates line profile variability as a function of phase as well as cycle-to-cycle modulation using CCF shape indicators BIS, FWHM, and normalized depth, with a special focus on the asymmetry parameter BIS. §3.3 describes in detail the phase variability of the metallic line velocity gradient as well as its cycle-to-cycle modulation and relation to BIS. Section 4 discusses possible astrophysical origins of the discovered behavior (§4.1), consequences for Cepheid RV measurements (§4.2), and implications for BW distance determination, in particular related to projection factors (§4.3). The final section 5 summarizes the results and concludes.

2 OBSERVATIONS, VELOCITIES & CCFs

2.1 *Coralie* monitoring campaigns

All data presented here are based on optical spectra of ℓ Carinae observed with the high-resolution ($R \sim 60\,000$) echelle spectrograph *Coralie* (Queloz et al. 2001a; Ségransan et al. 2010), which is mounted to the 1.2 m Swiss Euler telescope situated at La Silla Observatory, Chile. *Coralie*’s dedicated data reduction pipeline performs bias correction, flatfielding, and cosmic ray removal. The wavelength solution is supplied by a ThAr lamp. *Coralie* is housed in a thermally controlled room and any small intra-night variations in wavelength solution are corrected using reference spectra recorded simultaneously with the science exposure to reach single-digit m s^{-1} RV precision (e.g. Marmier et al. 2013).

Coralie has been upgraded twice over the course of the observations (2014 to 2016). Upgrades implemented in late 2014 are described in A16 and have had $\sim 15 \text{ m s}^{-1}$ impact on RV zero-point, which is only marginally relevant for the present work that deals with variations larger by one to three orders of magnitude. In mid 2015, the method for intra-night wavelength drift correction was changed. Formerly, the simultaneous wavelength reference was supplied by a ThAr lamp; now it is supplied by a Fabry–Pérot interferometer (FP), which further increased RV precision. The nightly wavelength calibration continues to be provided by a ThAr lamp, and the FP operates relative to this solution. Hence, no significant zero-point offset is expected, and none has been found thus far. A further exchange of *Coralie*’s CCD controller has also had no impact on the RV zero-point (F. Pepe and Geneva exoplanet group, priv. comm.) while reducing read-out time and improving noise properties.

This paper peruses *Coralie* spectra observed for two prior publications (A14: 2014 data, A16: 2015 data) as well as 230 new, as yet unpublished observations carried out between 2016 February 12 and 2016 May 10. Each of the three epochs (2014, 2015, 2016) considered here span two complete consecutive pulsation cycles. This allows to investigate cycle-to-cycle behavior as well as long-term changes in the RV and spectral variability.

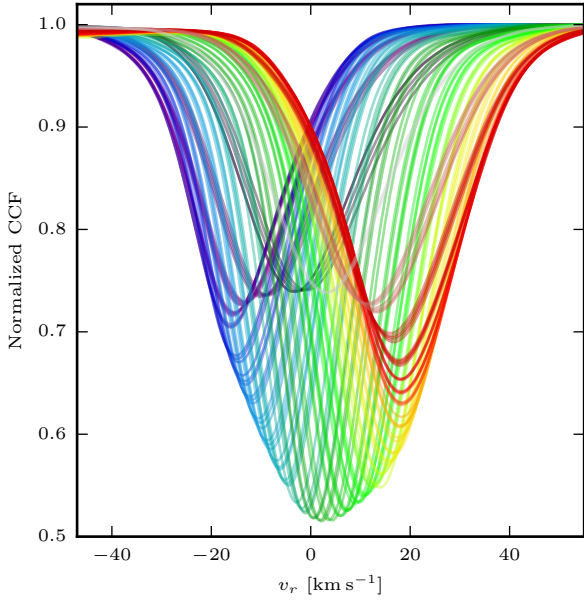


Figure 1. Cross-correlation functions (CCFs) calculated using a G2 line mask and data from the first complete 2016 cycle. Colors trace pulsation phase, the cycle proceeds from the top center counterclockwise.

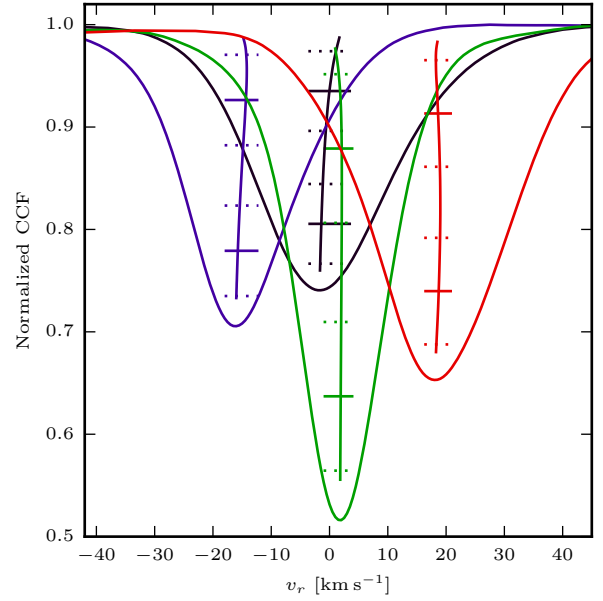


Figure 2. Illustration of the quantity BIS for four pulsation phases. BIS is the velocity difference (on the abscissa) between the CCF bisector (solid nearly vertical line) near its top and bottom, computed as the average of the regions included between horizontal dotted lines (Queloz et al. 2001b).

2.2 Cross-correlations and inferred RV

All RVs presented here are measured using the cross-correlation technique (Baranne et al. 1996; Pepe et al. 2002) and are expressed relative to the solar system barycenter. This technique cross-correlates a weighted numerical mask and the observed spectrum to produce cross-correlation functions (CCFs) based on which RV is measured by fitting Gaussian profiles. The line mask used for most Cepheid observations is representative of a solar spectral type (henceforth: G2 mask), and CCFs are computed such as to resemble absorption lines (for details, see Pepe et al. 2002). These velocities are referred to as “Gaussian RVs” with symbol v_r .

Figure 1 shows CCFs computed using the first fully sampled pulsation cycle of the 2016 campaign. The pulsation cycle proceeds counterclockwise and pulsation phase is color-coded to aid visual inspection. Fig. 1 clearly shows several phase-dependent features, including changes in: a) temperature (spectral type) via the varying depth of the CCF; b) RV associated with the pulsation via the displacement of the CCF along the abscissa; c) the width of the CCF; d) CCF asymmetry.

As a consequence of line asymmetry, RVs measured by fitting profiles such as Gaussian functions to CCFs (as well as to individual spectral lines) are biased (Burki et al. 1982) and much work has been done with the aim of improving the accuracy of Cepheid RV measurements by considering line asymmetry or different velocity curves of different spectral lines (e.g. Kraft 1967; Sasselov & Lester 1990; Wallerstein et al. 1992; Butler 1993; Kiss & Vinkó 2000; Nardetto et al. 2006; Gray & Stevenson 2007). Nevertheless, Gaussian RVs are extremely precise in that they are able to reproduce a consistent value under identical conditions, and this is illustrated by very smooth variations and small scatter when investigated appropriately (cf. A16). It is thanks to this precision that RV observations are now revealing previously unknown complexity in Cepheid pulsations.

This level of extreme RV precision should however not be confused with accuracy, i.e., the ability to reproduce the “true” value precisely. This is primarily because Cepheid atmospheres are highly dynamical and thus not characterized by a single velocity at a given phase. CCF-based RVs represent a weighted average RV of thousands of lines formed at different levels in the atmosphere and are therefore difficult to interpret in detail. However, even individual spectral lines are not free of such difficulty, since line formation in supergiant atmospheres occurs over significantly extended regions and is therefore more susceptible to the velocity field than in dwarf stars.

Despite these shortcomings, CCFs as well as RV curves based on them contain a great deal of useful information. In particular, CCF shape parameters exhibit smooth variations with phase due to the high SNR of CCFs and allow to investigate the relation between RV curve modulation and line profile variability. Specifically, this work considers—in addition to RVs—the CCFs’ full width at half maximum (FWHM) and normalized depth, both of which are measured by proxy via the fitted Gaussian profile. In addition, the quantity BIS (bisector inverse span) computed directly via CCFs serves as a proxy for line asymmetry. BIS is computed as the difference between average bisector velocities near the top 10–40 and bottom 60–90 % of the CCF, see Fig. 2 and Queloz et al. (2001b, Fig. 5).

Bi-Gaussian profiles have been proposed as an alternative to Gaussian profiles for measuring RV based on CCFs, specifically to take into account line asymmetry (Nardetto et al. 2006). To investigate how this different method of measuring RV on a given CCF reacts to cycle-to-cycle changes in the spectral line variability, bi-Gaussian RVs are determined for all CCFs employed in this

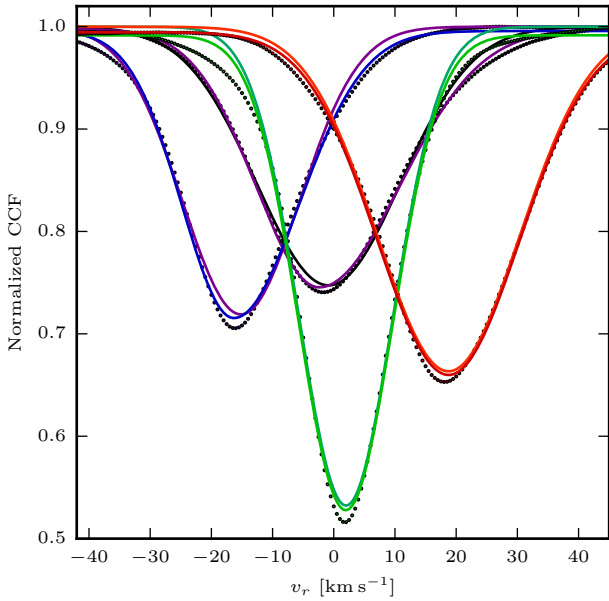


Figure 3. Illustration of Gaussian and bi-Gaussian RV profile fitting to CCFs of four different pulsation phases (selected as minimum radius, maximum expansion velocity, maximum contrast, and maximum contraction velocity). RV is defined as negative for objects approaching the observer.

work using the python implementation¹ by Figueira et al. (2013). Bi-Gaussian RVs are denoted by the symbol $v_{r,\text{biG}}$.

Figure 3 exemplifies the difference between a Gaussian and bi-Gaussian fit to four selected CCFs. Close inspection shows that bi-Gaussians do trace the computed CCF points more closely than a Gaussian fit. There does remain, however, a noticeable difference between the observed and fitted profiles. As a consequence of their tracing the CCF core more closely than Gaussians, bi-Gaussian RVs can be expected to lead to larger RV amplitudes.

2.3 Metallic line velocity gradient

It has been long known that Cepheid atmospheres are subject to significant velocity gradients (e.g. Sanford 1956; Kraft 1967; Dawe 1969; Karp 1973, 1978) and velocity differences among individual lines have been investigated in detail (e.g. Wallerstein et al. 1992; Butler 1993; Nardetto et al. 2007). In this work, a metallic line velocity gradient is computed using two newly-created correlation masks containing exclusively strong (depth > 0.65) and weak (depth < 0.55) lines, respectively. This procedure aims to exploit the benefit of the superior SNR of CCFs compared to individual lines in order to be maximally sensitive to cycle-to-cycle modulation. Both masks are based on the nominal solar (G2 spectral type) mask. The specific division between weak and strong line masks was adopted to achieve a similar weighting of the computed CCFs, i.e., $\sum_{i,\text{strong}} d_i \sim \sum_{i,\text{weak}} d_i$, where d_i denotes the line strengths as specified in the G2 mask. The weak-line mask thus contains 2030 lines, compared to 1209 lines in the strong-line mask.

Using strong and weak-line RVs measured by fitting Gaussian

profiles to CCFs computed using the strong and weak-line masks, the metallic velocity gradient is defined as

$$\delta v_r(t) = v_{r,\text{strong}}(t) - v_{r,\text{weak}}(t) - 0.641 \text{ km s}^{-1}, \quad (1)$$

with an offset of 0.641 km s^{-1} to correct for differential bias in the pulsation averaged velocities, cf. §3.1.2 and §3.2 as well as the well-known k -term problem (e.g. Nardetto et al. 2008). Uncertainties on $\delta v_r(t)$ are computed as the squared sum of each mask’s RV uncertainties.

$\delta v_r(t)$ defined in Eq 1 traces a velocity difference among lines formed at higher (stronger lines) and lower (weaker lines) levels in the Cepheid atmosphere (cf. Grossmann-Doerth 1994). $\delta v_r(t)$ thus indicates whether the region over which the gradient is valid is being compressed (positive δv_r) or stretched (negative δv_r) by the pulsation (as usual, RV is positive when receding from the observer). Table 1 succinctly summarizes this. Similar techniques have been employed for Mira stars to investigate shock propagation (Alvarez et al. 2001).

2.4 Variability with phase and modulated variability

This paper describes variations on different timescales, i.e., 1) variability over a pulsation cycle (alternatively: with pulsation phase, $P \sim 35.5 \text{ d}$) and 2) modulated variability, which denotes changes in the former variability pattern that occur over timescales longer than one pulsation cycle, ranging from one cycle to the next up to 2 years (baseline of the observations).

This work discusses differences between measurements on different timescales, i.e., data recorded 1) at the same time or 2) at the same phase during different pulsation cycles. The following notation is adopted to clearly distinguish these cases.

Differences of quantities observed *at the same time* are labeled as (lowercase) δ . For instance, the metallic line velocity gradient $\delta v_r(t)$ is the velocity difference of two different atmospheric layers measured using the same observed spectrum (cf. §2.3). Differences of quantities observed in *different pulsation cycles* are labeled using (uppercase) Δ . For instance, the difference in RV curve between two pulsation cycles is $\Delta v_r(\phi) = v_{r,\text{cycle2}}(\phi) - v_{r,\text{cycle1}}(\phi)$. In these cases, phase ϕ is computed using ephemerides determined in §3.1.1 below.

3 RESULTS

Figure 4 shows the Gaussian RVs measured during the three monitoring campaigns and illustrates the nomenclature adopted for each pulsation cycle as used in the following. Table 2 lists velocities and CCF shape parameters (cf. §2.2) for a subset of the observations; the complete data table is made publicly available online via the CDS². As mentioned in §2.2 v_r denotes RVs measured via Gaussian fits to CCFs computed using the G2 mask. Other RV definitions are clearly identified via their subscripts.

3.1 Cycle timing and modulated RV variability

3.1.1 Cycle timing

ℓ Carinae’s pulsation period fluctuates from one pulsation cycle to the next (e.g. A14, A16). Pulsation ephemerides are thus most pre-

¹ <http://bitbucket.org/pedrofigueira/line-profile-indicators>

² <http://cds.u-strasbg.fr/>

Table 1. Explanation of velocity difference in terms of compression and stretch within the atmosphere. Upper layers are traced by stronger (deeper) absorption lines, lower layers by weaker (shallower) lines. $\delta v_r = v_{r,\text{strong}} - v_{r,\text{weak}} - 0.641 \text{ km s}^{-1}$ (offset corrects for differential bias in v_γ for weak and strong line RVs).

Pulsational motion Velocity gradient	expansion ($v_r \lesssim v_\gamma$)	contraction ($v_r \gtrsim v_\gamma$)
$\delta v_r < 0$	upper layers expand faster: stretch	upper layers contract more slowly: stretch
$\delta v_r > 0$	lower layers expand faster: compression	lower layers contract more slowly: compression

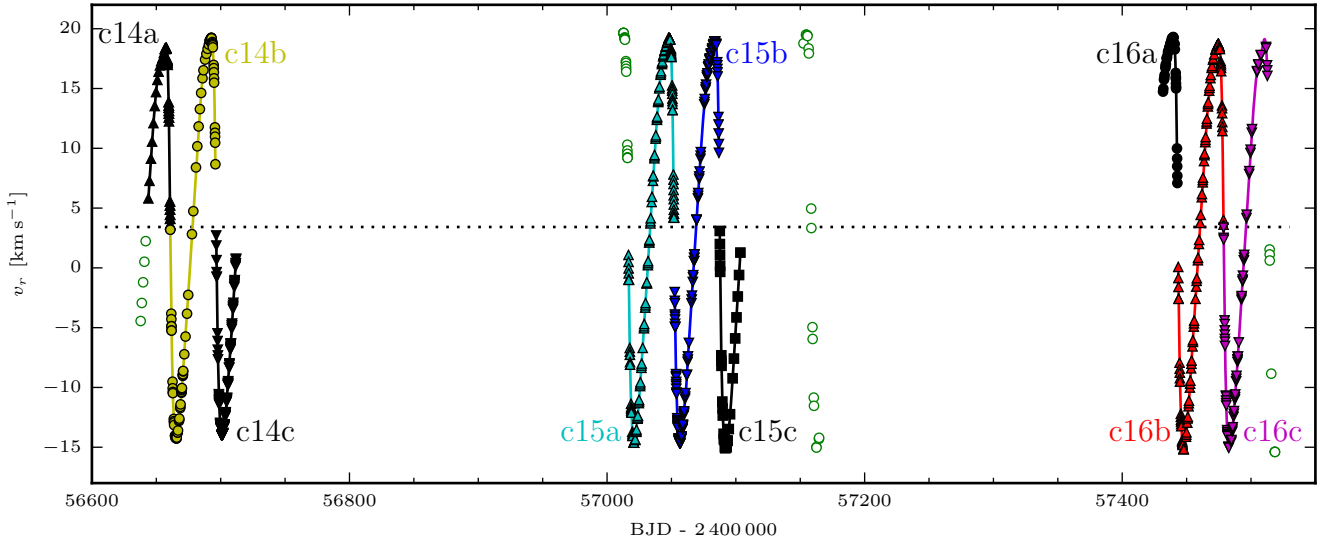


Figure 4. RV data of ℓ Carinae from the 2014, 2015, and 2016 campaigns. Individual pulsation cycles discussed in the following are marked here for comparison with all other figures. Green open circles show additional data not presented in detail in the following; these are also made publicly available. The horizontal dotted line represents $v_\gamma = 3.419 \text{ km s}^{-1}$ adopted to determine the duration of pulsation cycles.

cisely determined using the RV data of each individual pulsation cycle.

This work defines the start of a pulsation cycle to occur at minimum radius, since the steep RV variation during this phase allows for the most precise timing measurement (cf. [Derekas et al. 2012](#); [Anderson et al. 2016a](#)). Minimum radius, by definition, is reached when $v_r = v_\gamma$ while v_r is decreasing, with v_γ denoting the pulsation-averaged velocity. The main uncertainty related to timing the pulsation is therefore the ability to precisely define v_γ , since v_γ can exhibit erratic temporal variations due to the effects considered in this paper (see also A16). Furthermore, v_γ depends on the definition of RV employed (cf. §2.2), since v_γ is biased due to line asymmetry and different lines or measurement techniques differ in sensitivity to this bias. The most consistent way of timing the pulsation via RVs is therefore to determine v_γ separately for each type of RV definition. Fourier series fits with 13 harmonics to all available *Coralie* data thus yield $v_\gamma = 3.419 \text{ km s}^{-1}$ for Gaussian and $v_{\gamma,\text{biG}} = 3.441 \text{ km s}^{-1}$ for bi-Gaussian RVs based on the G2 mask, as well as $v_{\gamma,\text{strong}} = 3.571 \text{ km s}^{-1}$ and $v_{\gamma,\text{weak}} = 2.930 \text{ km s}^{-1}$. For the purpose of timing the pulsations, these are adopted as *true* values, although the (statistical) uncertainty of each of these pulsation-averaged velocities is on the order of 0.05 km s^{-1} . This comparison also illustrates the systematic difficulty of determining the absolute systemic velocity to better than a few hundred m s^{-1} .

Specifically, the duration of a pulsation cycle is determined as the time span between consecutive intersections of the spline-interpolated RV curve with v_γ at minimum radius. For the 2015

pulsation cycles, the timing specified in A16 is adopted. Table 3 specifies all cycle timings determined using Gaussian RVs.

Some of the available spectra were observed outside the date range of fully traced pulsation cycles. To make use of these data, *half-cycles* c14a, c14c, c15c, and c16a are defined as either beginning or ending at minimum radius. Since the duration of such half-cycles cannot be determined, a fixed pulsation period of 35.5 d is adopted to compute the corresponding pulsation phase. Throughout the paper, each cycle is plotted using a consistent scheme of colors and symbols as shown in Fig. 4. Half-cycles are drawn in black.

3.1.2 Modulated RV variability

Figure 5 illustrates ℓ Car's RV curve modulation in detail. It shows both Gaussian and bi-Gaussian RVs based on G2, weak-line, and strong-line correlation masks. The figure shows only the enlarged sections of the RV curve near minimum and maximum RV, since the modulated RV variability shows most clearly at these phases. Fig. 5 clearly demonstrates that RV curve modulation is exhibited regardless of the measurement method or line mask used, although its amplitude (or extent) depends on the definition of both.

Figure 5 also shows that cycle-to-cycle differences are seen in each of the three campaigns. However, Gaussian RVs from 2015 and 2016 reveal the tendency of longer-timescale modulations to be stronger than cycle-to-cycle modulations. 2014 data constitute an exception by differing particularly strongly between c14a and

BJD - 2 400 000 days	FWHM [km s ⁻¹]	BIS [km s ⁻¹]	depth [%]	v_r [km s ⁻¹]	$v_{r,\text{biG}}$ [km s ⁻¹]	$v_{r,\text{weak}}$ [km s ⁻¹]	BIS _{weak} [km s ⁻¹]	$v_{r,\text{strong}}$ [km s ⁻¹]	BIS _{strong} [km s ⁻¹]
56636.757136	17.4	0.384	41.7	-6.233 ± 0.015	-6.578	-6.223 ± 0.015	0.462	-6.397 ± 0.015	0.136
56637.848761	17.1	0.344	43.2	-4.445 ± 0.015	-4.758	-4.438 ± 0.015	0.405	-4.603 ± 0.015	0.084
56638.748377	17.0	0.318	44.3	-2.936 ± 0.015	-3.223	-2.947 ± 0.015	0.375	-3.073 ± 0.015	0.048
56639.774722	17.0	0.285	45.1	-1.205 ± 0.015	-1.463	-1.241 ± 0.015	0.346	-1.323 ± 0.015	-0.007
56640.769897	17.1	0.246	45.5	0.513 ± 0.015	0.286	0.445 ± 0.015	0.352	0.422 ± 0.015	-0.070
56641.766439	17.3	0.184	45.7	2.234 ± 0.015	2.061	2.120 ± 0.015	0.310	2.184 ± 0.015	-0.159
56643.842825	18.3	-0.003	45.1	5.809 ± 0.015	5.814	5.572 ± 0.015	0.071	5.873 ± 0.015	-0.342
56644.719386	18.8	-0.135	44.5	7.281 ± 0.015	7.41	6.993 ± 0.015	-0.130	7.406 ± 0.015	-0.429
56645.850598	19.6	-0.316	43.5	9.134 ± 0.015	9.431	8.756 ± 0.015	-0.422	9.336 ± 0.015	-0.563
56646.743305	20.4	-0.487	42.6	10.561 ± 0.015	11.024	10.109 ± 0.015	-0.713	10.821 ± 0.015	-0.710
...									
57512.458865	28.7	-0.476	29.0	16.941 ± 0.003	17.393	15.237 ± 0.007	-0.316	17.674 ± 0.004	1.196
57512.591455	28.8	-0.506	28.7	16.514 ± 0.005	17.001	14.755 ± 0.010	-0.340	17.269 ± 0.005	1.200
57512.708641	28.9	-0.543	28.4	16.057 ± 0.004	16.632	14.328 ± 0.009	-0.362	16.819 ± 0.005	1.289
57514.460114	28.2	1.159	25.1	1.539 ± 0.003	0.251	0.259 ± 0.006	-0.350	2.004 ± 0.003	1.285
57514.498343	28.1	1.169	25.2	1.125 ± 0.005	-0.192	-0.111 ± 0.012	-0.318	1.567 ± 0.006	1.375
57514.547207	28.0	1.208	25.2	0.614 ± 0.010	-0.729	-0.530 ± 0.022	-0.324	1.019 ± 0.012	1.380
57515.718169	25.9	1.185	25.2	-8.849 ± 0.004	-9.984	-9.247 ± 0.008	-0.306	-8.932 ± 0.004	1.421
57518.468137	23.3	1.246	27.4	-15.377 ± 0.004	-16.564	-15.492 ± 0.007	-0.289	-15.597 ± 0.004	1.436
57518.573887	23.2	1.229	27.5	-15.392 ± 0.003	-16.591	-15.499 ± 0.006	-0.297	-15.616 ± 0.003	1.509
57518.580913	23.2	1.233	27.5	-15.396 ± 0.003	-16.611	-15.515 ± 0.006	-0.299	-15.617 ± 0.004	1.485

Table 2. Example of the *Coralie* RV data used here. These data are based on observations taken in 2014 (A14), and 2015 (A16), as well as new data from a 2016 campaign. Measurements for the first and last 10 observations are shown. The full data set is made publicly available through the CDS. BJD denotes barycentric Julian date. Columns FWHM and depth are based on the Gaussian profile fitted to the CCF. BIS denotes bisector inverse span and is measured on the CCF. v_r is the RV measured via a Gaussian fit to the CCF computed using the G2 mask. $v_{r,\text{biG}}$ is analogously measured via a bi-Gaussian profile (Figueira et al. 2013). $v_{r,\text{weak}}$ and $v_{r,\text{strong}}$ denote RVs measured by fitting Gaussians to CCFs computed using weak- and strong-line correlation masks, respectively.

Cycle	BJD begin -2 400 000	BJD end -2 400 000	Duration [d]
c14a [†]	56642.448	56660.832	—
c14b	56660.832	56696.451	35.619
c14c [†]	56696.451	56713.398	—
c15a	57016.386	57051.957	35.571
c15b	57051.957	57087.491	35.534
c15c [†]	57087.491	57104.522	—
c16a [†]	57431.698	57443.184	—
c16b	57443.184	57478.681	35.497
c16c	57478.681	57514.278	35.597

Table 3. Timings of pulsation cycles via Gaussian RVs based on CCFs computed using the G2 mask. Phase is defined such that $\phi = 0$ at minimum radius. [†] marks incompletely traced pulsation cycles. Timings for 2015 data (c15a through c15c) are adopted from A16.

c14b near maximum RV. At minimum RV, the greatest difference seen is between c14c and c15c, followed by c14b and either of c16b or c. Near maximal RV, the overall greatest difference is seen for c14a and c16a, whereas the differences among all other cycles are much weaker.

Bi-Gaussian RVs mirror these variations closely during expansion (near minimum RV), albeit with greater amplitude. During contraction however, bi-Gaussian RVs exhibit different RV curve shapes with greatly amplified cycle-to-cycle differences. This behavior further strongly depends on the types of lines included in the CCF, with weak lines leading to much stronger cycle-to-cycle differences than strong lines due to enhanced asymmetry (§3.2).

3.2 CCF Variations

CCFs are frequently considered as representations of an average spectral line profile. However, this represents a crude approximation and does not account for the weighting of the spectral lines applied via the line masks, even for non-pulsating stars. In Cepheids, individual spectral lines are known to exhibit significant phase-dependent asymmetry. Moreover, these asymmetric lines formed at different depths are moving at different velocities due to the phase-dependent velocity field. All such lines are summed into a common CCF profile, whose detailed physical interpretation is thus complicated.

Nevertheless, certain features of the pulsations, such as temperature variations, are clearly evident in CCFs, see Fig. 1. Hence, CCFs do remain useful to investigate the variability of line profiles in Cepheids, although one must be careful to avoid over-interpretation of these variations. Of course, CCFs have the added benefit of very high SNRs, allowing to compare line profile variability even when the SNR per pixel of the spectra is rather low (down to spectral SNR of ~ 10).

Four quantities are used to describe CCF variability: 1) the difference between bi-Gaussian and Gaussian RVs ($v_{r,\text{biG}} - v_r$); 2) the bisector inverse span (BIS), cf. Sec. 2.2; 3) FWHM, the full width at half-maximum of the fitted Gaussian; 4) normalized CCF depth, i.e., the normalized peak height (here computed as a depth to resemble an absorption line) of the CCF. Figure 6 illustrates the variation of these parameters as a function of phase and their modulated (cycle-to-cycle and longer-term) character.

The difference between bi-Gaussian and Gaussian RVs based on a G2 mask varies between approximately -1.7 and 2.1 km s⁻¹. Conspicuously, this difference is opposite to the BIS variation and has nearly identical amplitude. This correspondence is a consequence of the bi-Gaussian's construction as an asymmetric line

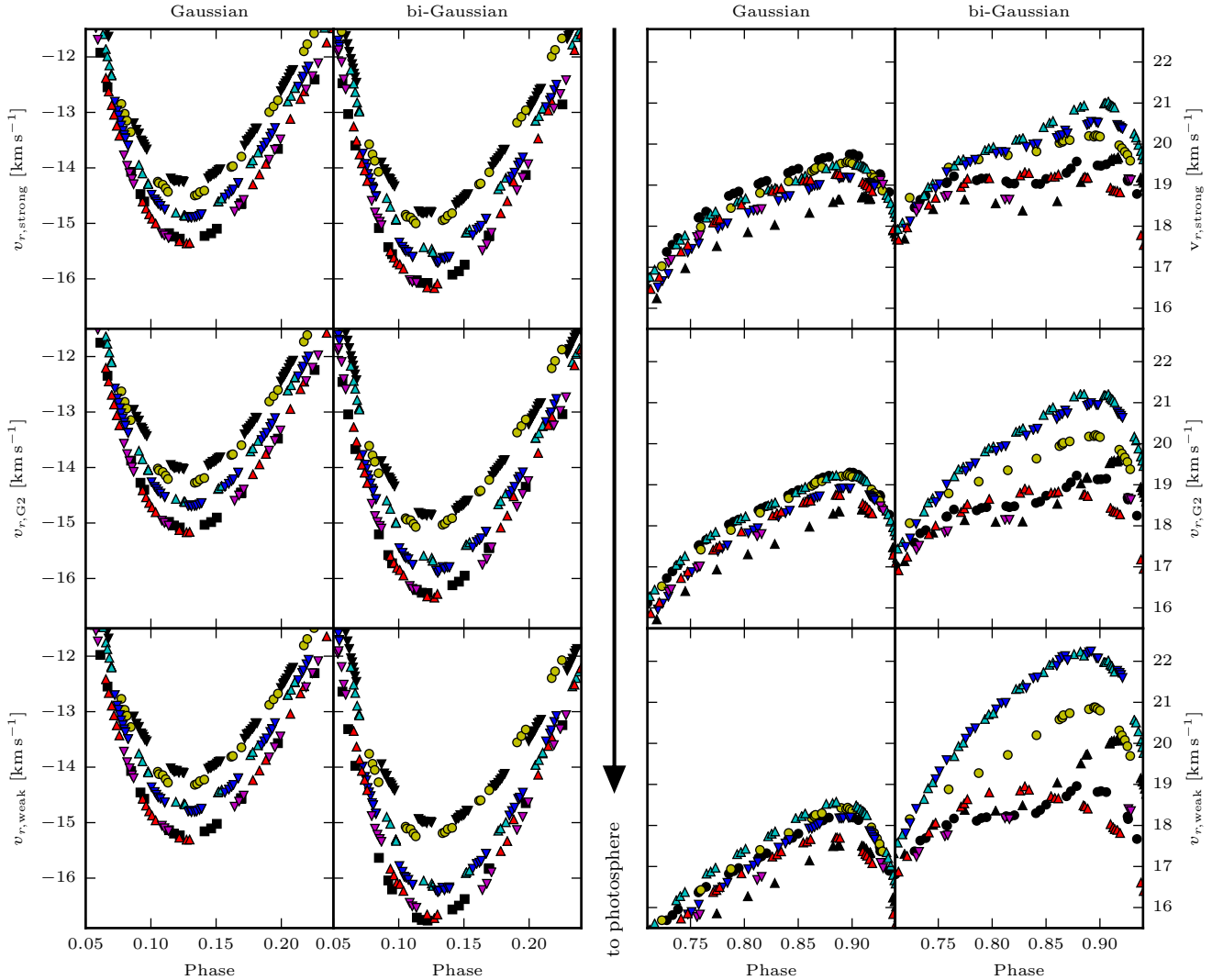


Figure 5. Modulated RV variability near minimum (left-hand side) and maximum (right-hand side) velocity based on lines formed at different heights in the atmosphere as measured using Gaussian and bi-Gaussian profiles. RVs shown are based on strong lines in *top panels*, the default G2 mask in *center panels*, and weak lines in *bottom panels*. Symbols distinguish between the pulsation cycles, cf. Fig. 4. Statistical errors are smaller than symbol size.

profile. BIS is defined such that it is negative when the line core is red-shifted compared to the higher sections of the CCFs, ergo the bi-Gaussian RV for a negative BIS is larger than the Gaussian RV, and vice versa for positive BIS (core more blue-shifted than upper CCF regions). As Figure 7 shows, there is a near one-to-one correspondence between $v_{r,\text{biG}} - v_r$ and the BIS parameter for all pulsation cycles. Linear regressions assuming a fixed intercept at (0,0) yield slopes between -0.94 and -1.07 for the individual pulsation cycles, whereas a regression to all data has slope -1.009.

The primary origin of spectral line asymmetry in Cepheids are rotation (Gray & Stevenson 2007) and velocity fields (e.g. Karp 1975; Nardetto et al. 2006). The rotational contribution to line asymmetry originates in the convolution of the rotation profile and the pulsation velocity. Thus, the rotational contribution to BIS is strongest, when the pulsation velocity is extreme (minimal or max-

imal), and this overall pattern is clearly observed in the BIS parameter.

The surface rotation velocity v_{eq} of a Cepheid is expected to vary by up to 10 % over the course of an expansion-contraction half-cycle due to conservation of angular momentum (Gray & Stevenson 2007). However, since the greatest difference in v_{eq} occurs at minimum and maximum radius where the pulsational velocity vanishes, no significant contribution to BIS is expected due to this effect.

The contribution of pulsation-induced velocity fields to line asymmetry can be understood as the added contributions of line forming regions moving at different velocities. For instance, if higher layers are expanding more quickly than lower ones, positive BIS is to be expected. Conversely, negative BIS is expected when deeper layers are contracting more slowly than higher layers. The steep sign reversal near minimal radius ($\phi \sim 1$) is thus a conse-

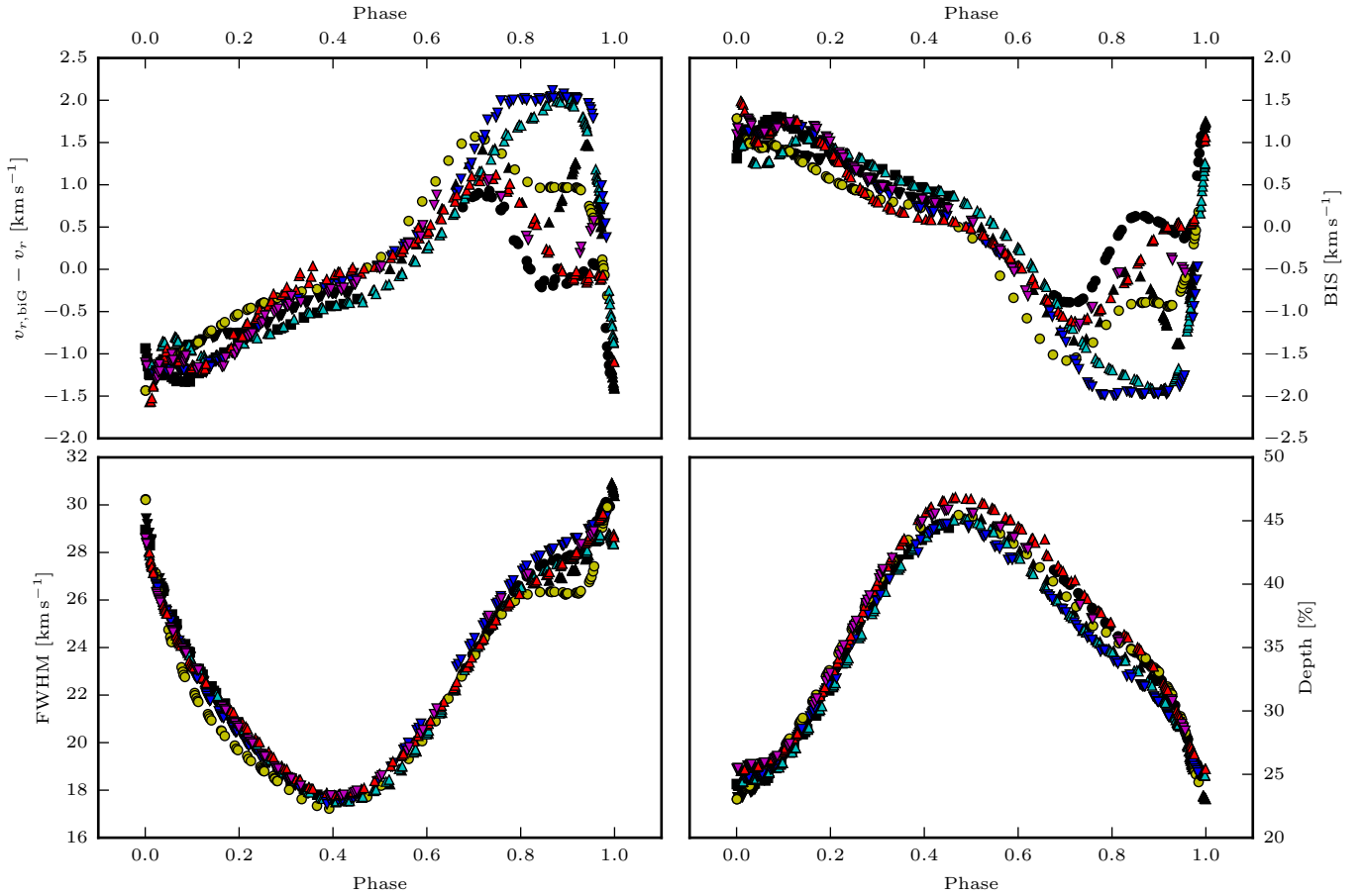


Figure 6. Variation of CCF shapes with pulsation phase. *Top left:* Difference of bi-Gaussian and Gaussian RV, *top right:* Bisector inverse span (BIS), *bottom left:* FWHM of fitted Gaussian, *bottom right:* Depth in percent of fitted Gaussian.

quence of the outward-directed shock wave reversing the velocity gradient. These relationships are further investigated in §2.3.

In (non-variable) cool supergiants, velocity fields due to granulation create significant line asymmetry, with bisectors exhibiting a smooth variation as function of spectral type. Full bisector velocity spans (top minus bottom) range from $\sim 300\text{--}500\text{ m s}^{-1}$ near G4 (less at K2) up to ~ -1 to -2 km s^{-1} near F5–F8 (Gray & Toner 1986). Intriguingly, the granulation-induced bisector asymmetry of non-variable supergiants has opposite sign from the BIS variations shown in Fig. 6, even though ℓ Car’s variability spans similar spectral types. BIS is positive when ℓ Car is hottest (maximal RV), and BIS is negative when it is coolest (after maximal radius). Thus, it appears that granulation is not the likely origin of ℓ Car’s observed line asymmetry.

The variation of parameter BIS in Figure 6 exhibits several noteworthy peculiarities. First, the steep rise immediately before phase 1.0 is the most consistent part among the different pulsation cycles. The outward-directed pulsation wave initiated by the main pulsation mechanism (the He II partial ionization zone) is undoubtedly responsible for this feature, since it occurs very close to minimal radius. The occurrence of this significant realignment further supports the choice of v_γ as reference point for timing the duration of individual pulsation cycles (§3.1.1). Second, BIS reaches

more extreme values during contraction ($\phi \sim 0.8\text{--}0.9$) than during expansion ($\phi \sim 0.1\text{--}0.2$) during some pulsation cycles (c15a and b). Third, while cycle-to-cycle differences in BIS are evident at all phases, they are most strongly pronounced during contraction and exhibit a wave-like pattern that differs from cycle to cycle, is not in phase with the pulsation, and carries over into subsequent pulsation cycles. Thus, the atmospheric velocity field during a given cycle retains a memory of the previous cycle. Fourth, BIS modulation is more noticeable on longer timescales than among subsequent cycles, possibly suggesting (semi-)periodicity, given that the 2014 and 2016 cycles are more similar to each other than to the 2015 cycles. A periodicity of this timescale (~ 2 years) would be consistent with the order of magnitude expected for the rotational period of a $\sim 180 R_\odot$, $9 M_\odot$ Cepheid (Kervella et al. 2004; Anderson et al. 2014, 2016b).

The modulated variability of the BIS parameter provides a crucial insight into the origin of RV curve modulation. As explained in Sec. 2, RV measurements obtained by fitting Gaussian profiles to CCFs are biased (Burki et al. 1982). However, if the shape of spectral lines at a fixed phase were to repeat perfectly, then Gaussian RVs would be subject to the same bias in each pulsation cycle and thus yield consistent results at fixed phase. The modulated BIS variability here discovered demonstrates that line shapes are

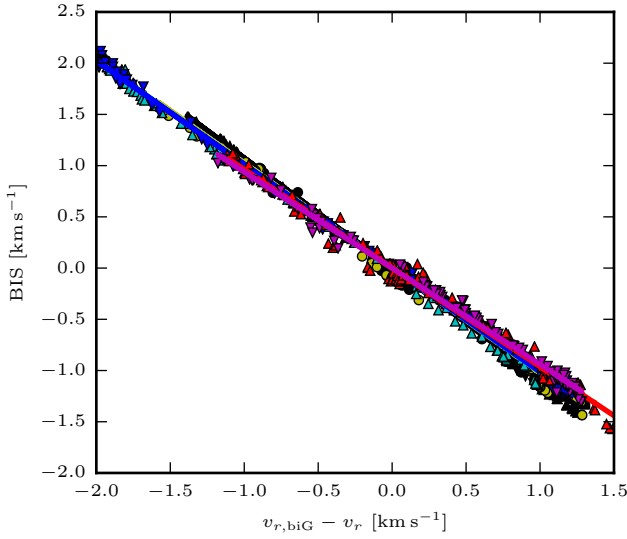


Figure 7. Bi-Gaussian RV offset against bisector inverse span (BIS) determined from the CCF. Each cycle is fitted separately, the average slope over all cycles is -1.009 .

not consistent between pulsation cycles, thus leading to RV curve modulation. Bi-Gaussian RVs are even more strongly affected by these cycle-to-cycle differences in line shape, as expected due to their asymmetric construction (cf. Figs. 5 and 7). This link between line asymmetry, velocity gradients, and RV curve modulation is explored in detail using a Doppler tomographic method in §3.3.

Figure 6 further reveals peculiar differences in the FWHM and CCF depth parameters among pulsation cycles. As was the case for BIS, the most conspicuous differences are seen near pulsation phase 0.9. Line width at these phases has previously been discussed in terms of shock-induced turbulence (e.g. Karp 1973; Fokin et al. 1996). The cycle-to-cycle variations of the FWHM parameter do not directly correlate with those exhibited by BIS, cf. yellow circles and blue downward triangles, for instance.

Figure 8 complements Fig. 6 by illustrating the variability of CCF shape parameters BIS, FWHM, and CCF depth as a function of v_r , centered on v_γ . In particular, this reveals butterfly-shaped diagrams for BIS (and thus also the $v_{r,biG} - v_r$ difference). Figure 8 features smooth variations that differ noticeably among the pulsation cycles. It clearly shows that BIS tends to be most extreme when RV is extreme, which illustrates the significant impact of surface rotation on line asymmetry. An important exception to this general behavior is the peak with positive BIS near the top center of the plot, during expansion. This phase coincides with the piston phase of the pulsation, when velocity gradients are expected to be strongest due to the outward-directed pulsation wave passing through the atmosphere. The variation of FWHM is also most disturbed near minimum radius ($v_r \sim v_\gamma$ and maximal FWHM).

Figure 9 shows the computed BIS and RVs for both the weak and strong-line CCFs, in analogy with the upper right panel of Fig. 8. The resulting BIS loops are significantly different for strong and weak line CCFs. Several interesting features appear in these diagrams. Firstly, BIS_{weak} variations reach much more extreme negative values at maximum velocity than BIS_{strong} . This is further illustrated by Fig. 10. Secondly, observed cycle-to-cycle differences in BIS are largest at maximum RV, just as the observed differences in

v_r . Thirdly, BIS_{weak} exhibits more intense modulation than BIS_{strong} , which also matches the RV curve modulation seen in Fig. 5. For strong line CCFs, these loops differ more strongly at every point along the duty cycle compared to weak line CCFs, although the differences at the extremes is less pronounced. For instance, c15a yields a much more compact loop than c16b. Strong line loops (BIS_{strong} vs. $v_{r,strong}$) are much more open during expansion than weak line loops, for which the opposite appears to be the case.

The loops in Figure 9 exhibit the widest opening when $v_r \sim v_\gamma$, i.e., close to times of extremal radius. The closer and steeper correlation between BIS_{weak} and $v_{r,weak}$ compared to the same quantities derived for strong line CCFs is peculiar and may be indicative of depth-dependent differential rotation, since line asymmetry is in large parts due to the convolution of the rotation and pulsational velocities.

Besides rotation, velocity fields contribute significantly to line asymmetry. The relationship between the metallic velocity gradient and BIS parameter is therefore investigated in detail in the following §3.3.

3.3 Velocity Gradients

Cepheid atmospheres are highly dynamic and characterized by strong velocity fields. Previous work has shown in detail the different velocities exhibited at fixed phase for spectral lines belonging to different elements, ionization potentials, and line depths (e.g. Sanford 1956; Karp 1978; Sasselov et al. 1989; Sasselov & Lester 1990; Wallerstein et al. 1992, 2015; Butler 1993; Nardetto et al. 2006, 2007; Hadrava et al. 2009).

The metallic line velocity gradient, $\delta v_r(t)$, is computed here as the difference between strong-line and weak-line RVs as defined in Eq. 1 to investigate the relationship between the BIS parameter and the atmospheric velocity field. The key benefit of the presently used definition of $\delta v_r(t)$ is its ability to reveal even small differences (both at the same time and between different pulsation cycles) thanks to the very high RV precision afforded by the cross-correlation technique.

However, the present approach is also limited by several choices, including blurring due to the inclusion of many spectral lines formed at different heights for each mask, the approximate nature of using spectral lines of different strength to trace different atmospheric layers, and the possible influence of different portions of the stellar disk being probed by different line masks. Nevertheless, this approach is useful and tests performed using different line selections revealed similar trends, albeit with different amplitudes.

Figure 11 illustrates δv_r (center panel) against pulsation phase together with the RV curves (v_r , top panel) and the BIS variation (bottom panel). The dependence of δv_r on BIS is further shown in Fig. 12.

Figure 11 reveals a globally smooth variation of the velocity gradient as a function of pulsation phase that is dominated by three humps of increasing amplitude located at phases of approximately 0.25, 0.77, and 0.97. A first minimum before the first hump at phase 0.1 – 0.15 coincides with the peak of the RV curve, i.e., where the shock wave emerges from below. The slight hump indicating reduced stretch thus appears to be related to the trailing part of this shock wave.

Shortly after maximum radius (at phase ~ 0.6), δv_r turns over from negative to positive values as the star is contracting. This compression first proceeds in an accelerated fashion until a maximum is reached near phase 0.77 and the compression is slowed temporarily before being re-accelerated forcefully towards the highest peak

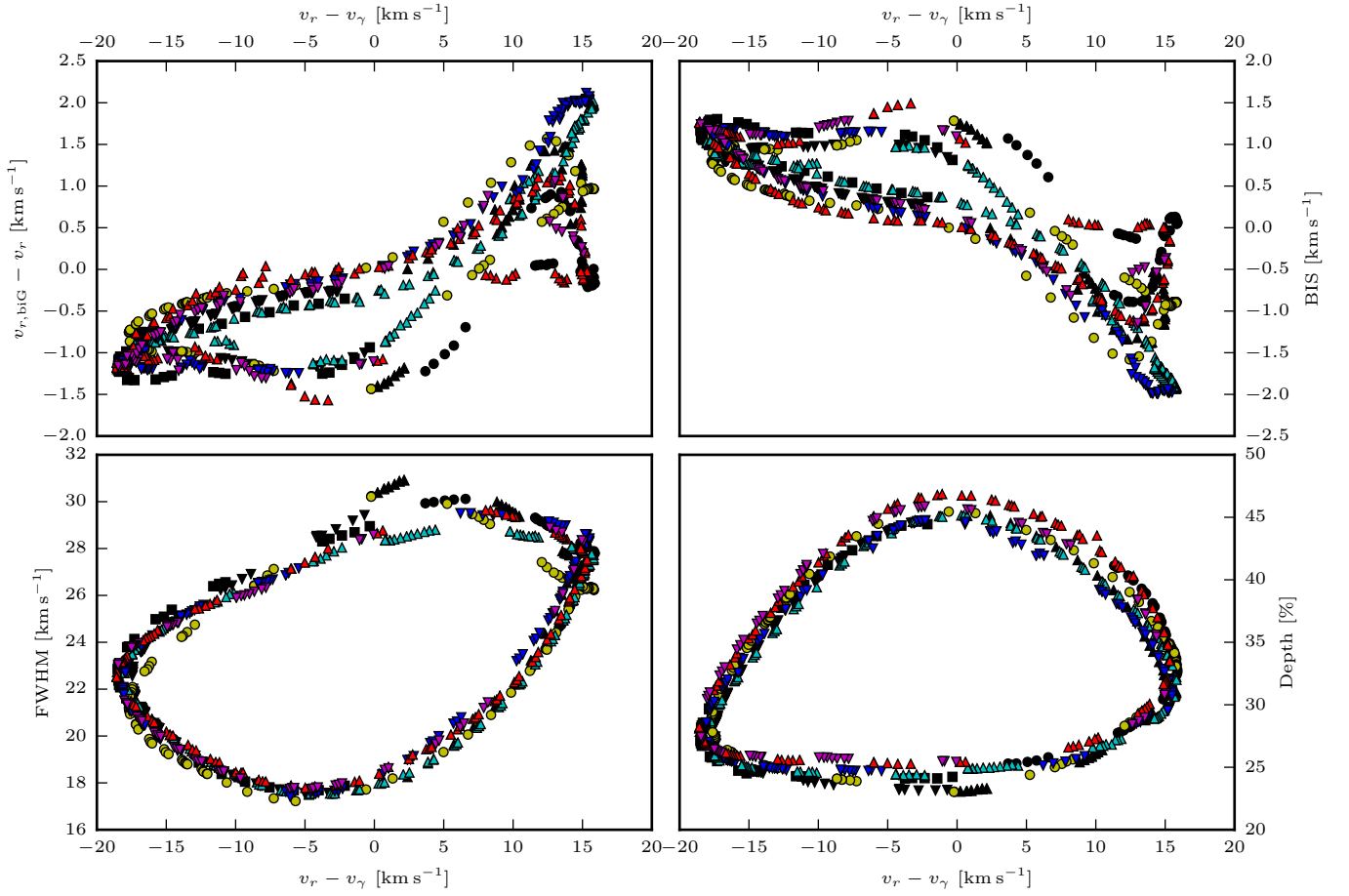


Figure 8. Variation of CCF line shape parameters against RV, shown here centered on the pulsation-averaged velocity v_γ . *Top left:* bi-Gaussian minus Gaussian RV, *top right:* Bisector inverse span (BIS), *bottom left:* FWHM of fitted Gaussian, *bottom right:* Depth in percent of fitted Gaussian.

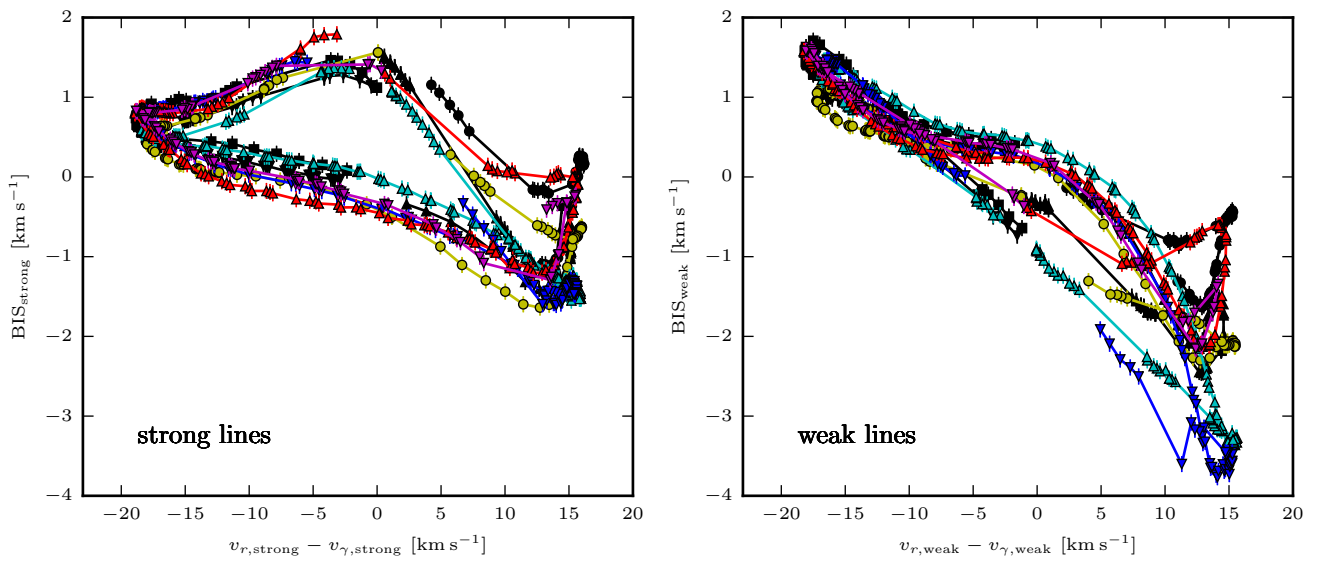


Figure 9. BIS against RV for strong-line CCFs (left-hand panel) and weak-line CCFs (right-hand panel). Weak lines exhibit a broader range of asymmetry than strong lines and are subject to stronger modulations near maximal velocity (fastest contraction).

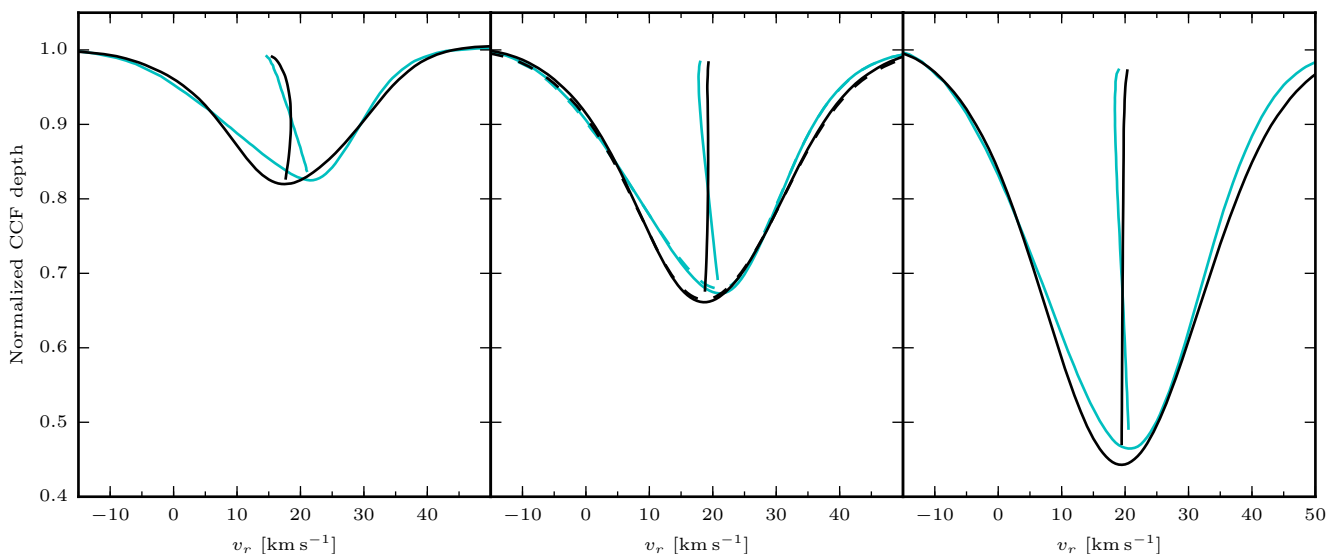


Figure 10. Difference in CCF shape at nearly identical phase as observed in c15a ($\phi = 0.869$, cyan) and c16a ($\phi = 0.876$, black) where the difference in BIS is maximal among pulsation cycles, cf. Fig. 6. Left-hand panel shows weak-line CCFs, right-hand panel strong-line CCFs. Center panel shows CCFs based on G2 mask as solid lines as well as the summed weak and strong-line CCFs as dashed line. Line bisectors are shown for each mask computed.

near phase 0.97. The variation of δv_r between phase 0.75 and 0.95 (well before minimum radius is reached) is indicative of a process beyond gravitational collapse that first works against the acceleration of compression and subsequently contributes to it. This is certainly a feature of the pulsation mechanism, given that it is apparent during every pulsation cycle.

Finally, near phase 0.95-0.98, δv_r is reminiscent of a discontinuity and experiences a sharp turnaround, proceeding from maximal compression to maximum stretch in less than 10% of a pulsation period. This feature coincides with the very fast decrease in RV, cf. Fig. 5, which initiates the expansion.

Figure 11 also reveals the existence of significant cycle-to-cycle changes in δv_r . The most striking differences among pulsation cycles take place during contraction, start near $\phi = 0.6$, and proceed until expansion is initiated. This behavior is analogous to the greater extent of RV curve modulation observed during contraction (near maximum RV). Smaller cycle-to-cycle differences near minimum RV (phase 0.1 – 0.15) further coincide with lower RV curve modulation at minimum v_r . δv_r also exhibits more consistent behavior for intermediate phases during which little to no cycle-to-cycle v_r modulation is found.

The smooth variation of the each cycle's δv_r curve demonstrate that the present approach traces even small changes in velocity gradients with confidence. Similarly to the behavior of RV curve modulation, consecutive pulsation cycles tend to reproduce similar δv_r variability, whereas longer timescales lead to larger differences. Differently from the RV curve (Fig. 5), however, the 2014 and 2015 cycles are more similar to each other than to the cycles observed in 2016. These different modulation patterns among the various spectral indicators suggest a highly complex behavior of modulated line profile variability across all spectral lines.

Comparing cycle-to-cycle changes in δv_r with those observed for BIS in the bottom panel of Fig. 11 shows both indicators to correlate very closely. For instance, close to phase 0.1 (near fastest v_r), c15a exhibits both lowest BIS and lowest δv_r , whereas c16b exhibits greatest BIS and δv_r . Close to phase 0.8, c16a yields the

highest value for δv_r and BIS, and similarly, c15b exhibits minimal BIS and δv_r . However, the correspondence is not perfect and some smaller differences remain. The need to adopt a common value for v_r for all pulsation cycles for timing purposes (cf. §3.1.1) likely dominates these small differences. Further reasons for non-correspondence include the fact that BIS is measured on CCFs computed using the G2 mask, which contains some spectral lines not included in the strong and weak line masks (depth range 0.55 – 0.65). However, this contribution is expected to be small, since the addition of weak and strong-line CCFs closely resembles G2 mask-based CCFs (cf. Fig. 10).

Figure 12 illustrates another important feature, namely that variations in δv_r and line asymmetry (BIS) correspond more closely during expansion ($\delta v_r < 0$) than during contraction ($\delta v_r > 0$). This points towards a resetting effect of the outward-directed pulsation wave. Other atmospheric effects such as convection and turbulence appear to cause greater departures from this correspondence once the shock wave has passed through the atmosphere.

Figures 13 and 14 serve to further illustrate the correspondence between modulated BIS and δv_r . Figure 13 shows this behavior as a function of phase, whereas Fig. 14 plots $\Delta \delta v_r$ against ΔBIS . It is worth recalling here the nomenclature adopted where δ indicates the difference between measurements obtained at the same time and Δ denotes differences between pulsation cycles. Both figures use pulsation cycle c15a as a reference to compute cycle-to-cycle differences. The amplitude of ΔBIS is approximately a factor of 3 larger than the amplitude of $\Delta \delta v_r$, most likely due to the difference in spectral lines between the G2 mask used to compute BIS and the fewer and different lines used to compute weak and strong line CCFs. For $\Delta \delta v_r$, the maximal difference among 2016 and 2015 pulsation cycles reaches $\sim 700 \text{ m s}^{-1}$, which is on the order of 50% of the average δv_r at the same phase ($\phi \sim 0.875$). For BIS, cycle-to-cycle differences reach up to $\sim 2.1 \text{ km s}^{-1}$ at this phase, with BIS ranging from +0.1 to -2.0 km s^{-1} .

The correspondence between the shape of the $\Delta \delta v_r$ and ΔBIS curves against phase (Fig. 13) is striking and demonstrates that

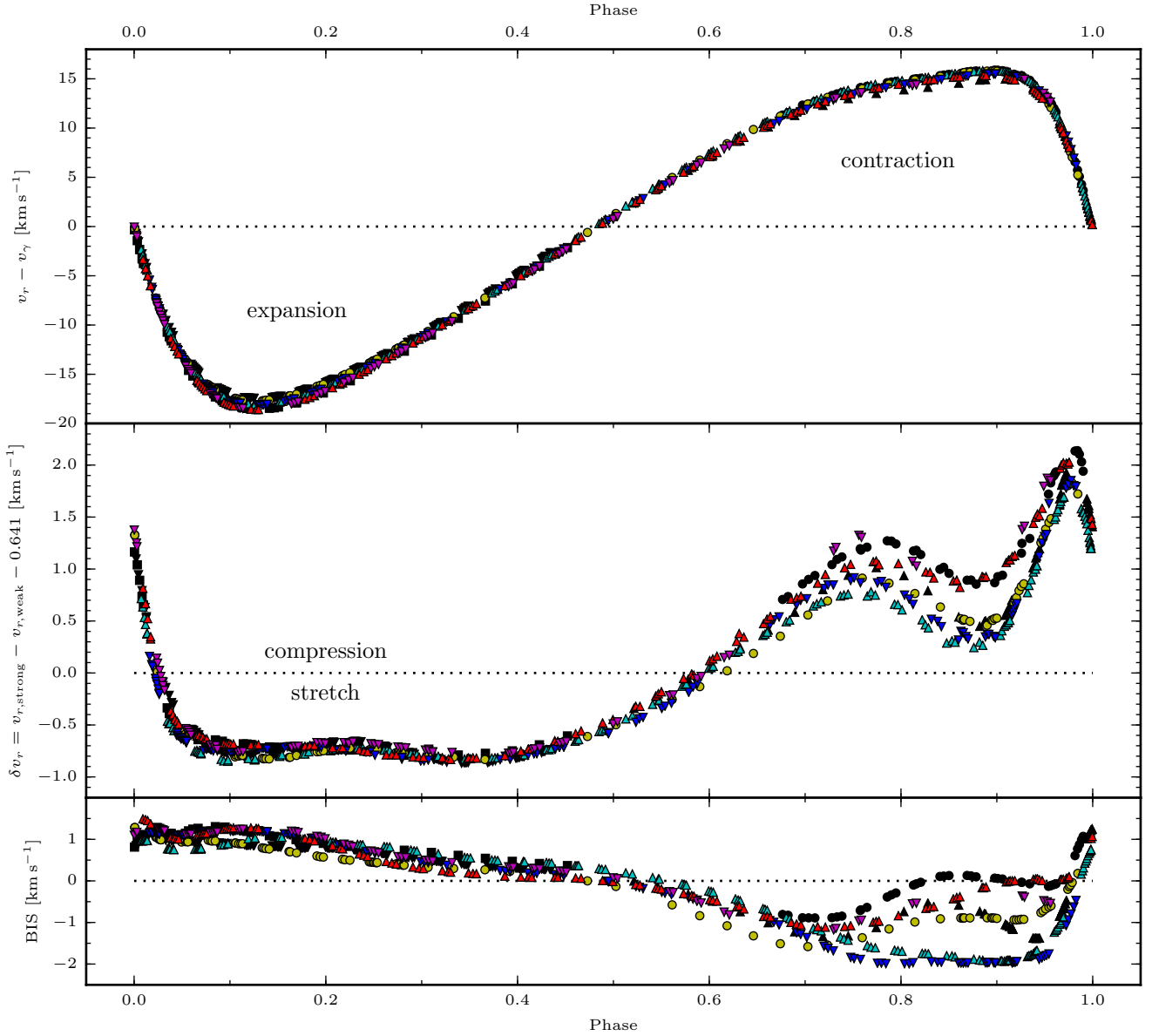


Figure 11. Time-dependent velocity gradients δv_r (center) and their correspondence to the overall RV variability v_r (top) and the bisector inverse span (BIS, bottom). $\delta v_r > 0$ indicates compression, cf. Tab. 1. Velocity gradients and line asymmetry are clearly correlated, both exhibit patterns that are more similar in 2014 and 2016 than in 2015.

cycle-to-cycle and longer-term changes in the velocity gradient are primarily responsible for the observed modulated BIS variability. This important result suggests that cycle-to-cycle RV curve modulation in long-period Cepheids discovered by A14 is primarily due to cycle-to-cycle and longer-term variations in velocity gradients that modify the spectral line variability, acting primarily on line asymmetry. Despite a remarkable correspondence between the parameters, Fig. 13 also shows that Δv_r does not correlate immediately with changes in the velocity gradient ($\Delta \delta v_r$). This is likely due to the combined influence of line profile variations on FWHM, depth, and BIS, of which only BIS was considered here. Further research is required to test whether such correlations could be used to

reduce the impact of modulated line profile variability on Cepheid RV measurements.

Since cycle-to-cycle changes in velocity gradient correlate with those in BIS, it follows that BIS can serve as a suitable proxy to detect changes in velocity gradients. This is particularly useful to extend the investigation of cycle-to-cycle differences to fainter stars, for which the here presented Doppler tomographic technique cannot be applied due to insufficient spectral SNR. Specifically, investigation of BIS can help to distinguish between time variations in the pulsation averaged velocity v_r due to spectroscopic binarity (no cycle-to-cycle difference in BIS) and modulated line shape variability. This is useful to detect companions with low mass ra-

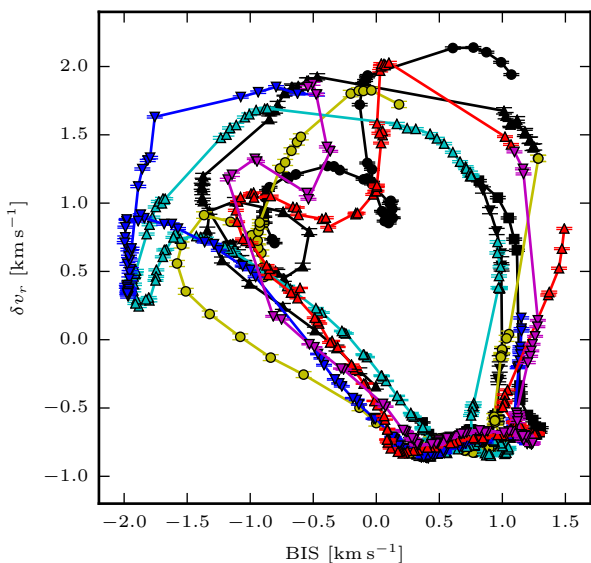


Figure 12. Velocity gradient δv_r against CCF asymmetry parameter BIS. δv_r corresponds more closely to BIS when $\delta v_r < 0$, i.e., when the atmosphere is being stretched.

tios (such as δ Cep’s spectroscopic companion, see [Anderson et al. 2015](#)).

4 DISCUSSION

The above results reveal a first insight into the highly complex modulated line profile variability of Cepheids. This work has focused on quantities accessible via CCFs in order to start exploring the origin of RV curve modulation discovered recently (A14). Work in progress will expand this investigation to individual spectral lines. It should be noted that RV curve modulation in short and long-period Cepheid occurs on different timescales. Hence, the following discussion of the above results should apply primarily to Cepheids with pulsation periods on the order of 20–60 d. Further research is required to investigate how these phenomena translate to other Cepheids and/or period ranges.

4.1 On CCF asymmetry and velocity gradients

The preceding sections have revealed a highly complex and cycle-dependent line profile variability. Although this paper is purely observational, it is useful to summarize the key results capable of informing the astrophysical interpretation of the observed modulations. The most important clues found here include (in arbitrary order):

- (i) pulsation cycles retain memory of the preceding cycle;
- (ii) long-term modulation tends to dominate over short-term modulation;
- (iii) there is tentative evidence for a repetition in BIS modulation (2014 compared to 2016 data);
- (iv) Δ BIS correlates closely with $\Delta\delta v_r$;
- (v) the strongest cycle-to-cycle differences in δv_r occur during contraction, well before minimal radius;

(vi) the asymmetry of weak lines more strongly correlates with pulsational velocity than for strong lines;

(vii) weak lines show greater asymmetry and exhibit greater cycle-to-cycle modulation than strong lines.

Changes in the velocity field could be explained by several mechanisms, including convection, additional (e.g., non-radial or strange) pulsation modes, surface inhomogeneities (spots), or inelastic shock. Granulation has previously been mentioned as a possible explanation for so-called “period-jitter” in Cepheids ([Neilson & Ignace 2014](#)). As mentioned in §2.3 however, granulation-induced line asymmetry in non-variable supergiants has opposite sign of ℓ Car’s line asymmetry. Hence, other asymmetry-inducing effects such pulsation-induced velocity gradients and rotation complicate the assessment of granulation based on line asymmetries. Multi-dimensional models of pulsation-convection interactions ([Mundprecht et al. 2013, 2015](#)) should provide interesting insights into this possible explanation. Convective perturbations of the velocity field are likely to occur, since convective cells in cool supergiants are large and ℓ Car is a particularly cool Cepheid. Δ BIS is particularly strong when ℓ Car is coldest, further corroborating a link with convection.

Rotation and associated magnetic phenomena are an interesting possibility primarily because of the tentative evidence of a pattern repeating over a 2-year timescale, which is broadly consistent with the expected rotation period of ℓ Car. In addition, the dependence of line asymmetry on formation height indicates possible differential (depth-dependent) rotation. While a magnetic origin of amplitude modulations has been suggested ([Stothers 2009](#)), little is known observationally about the magnetic fields of Cepheids (see e.g. η Aql in [Grunhut et al. 2010](#)). Inhomogeneities in the velocity field of ℓ Car’s surface (e.g. due to spots) could lead to line asymmetries similar to those observed in other rotating stars ([Deutsch 1958](#); [Goncharskii et al. 1977](#); [Toner & Gray 1988](#)).

Shock associated with the pulsation has received much attention in the literature (e.g. [Karp 1975](#); [Schmidt & Parsons 1984](#); [Böhm-Vitense & Love 1994](#); [Mathias et al. 2006](#); [Engle et al. 2014](#); [Neilson et al. 2016](#)). Unresolved, time-dependent line-splitting via the [Schwarzschild \(1952\)](#) mechanism could introduce line asymmetry, which, if the shock were inelastic, could change from one cycle to the next and affect the velocity field. Line splitting and emission of the shock-sensitive Ca II K line in ℓ Car was previously reported [Dawe \(1969\)](#) and is also seen at certain phases in the *Coralie* spectra, together with emission in H α . Furthermore, UV emission observed at certain phases has been linked to shock for ℓ Car ([Schmidt & Parsons 1984](#); [Böhm-Vitense & Love 1994](#); [Neilson et al. 2016](#)). The strong BIS modulation occurring during contraction could be related to such inelasticity, or may be indicative of additional (e.g. higher-order or non-radial) pulsation modes.

At present, these considerations remain of course speculative. Future work involving additional stars, individual line profiles, and broader coverage of the electromagnetic spectrum will allow additional insights into the complexity of Cepheid pulsations.

4.2 Implications for Cepheid RV measurements

As shown in this paper, ℓ Car’s line profile variability (LPV) is subject to modulation between consecutive pulsation cycles as well as on longer timescales. Since RVs are measured via the Doppler shift of spectral lines, it is clear that RV curve modulation is a symptom of cycle-to-cycle changes in LPV.

In general, the concept of a single radial velocity is ill-defined

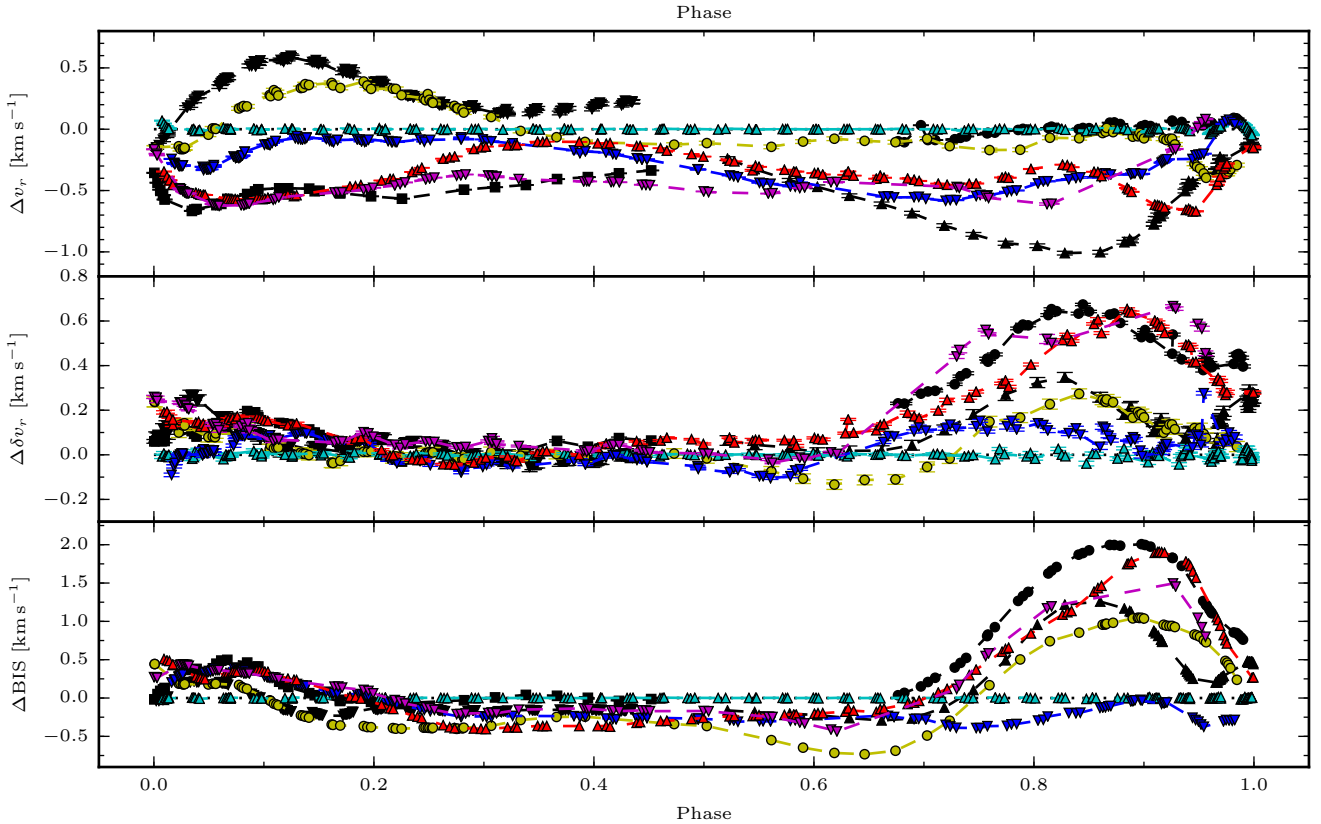


Figure 13. Cycle-to-cycle and longer-term changes in RV, Δv_r (top), velocity gradient, $\Delta \delta v_r$ (center), and CCF asymmetry parameter ΔBIS (bottom) shown relative to c15a (cyan upward triangles). Differences among cycles seen in δv_r and BIS correlate closely, indicating that BIS is a suitable proxy to trace velocity gradients. Changes in v_r do not mirror directly the changes in velocity gradient or BIS.

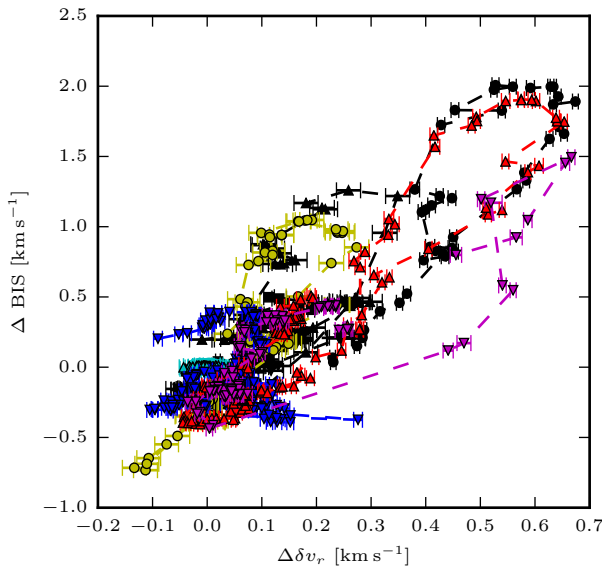


Figure 14. Cycle-to-cycle changes in velocity gradient δv_r against those exhibited by BIS calculated relative to Fourier series fit to c15a data.

for a Cepheid due to well-known velocity gradients (e.g. Sanford 1956; Dawe 1969; Wallerstein et al. 1992; Butler 1993; Nardetto et al. 2007). While velocity gradients may bias individual RV measurements, they do not preclude the recovery of the true pulsational variability if such bias can be accounted for, e.g. via (phase-dependent) projection factors, see also §4.3. However, this work shows that the phase variability of velocity gradients does not repeat perfectly between pulsation cycles, leading to a complex time-dependence of RV variability. This problem is analogous to the difficulties encountered by RV-based planet searches, where stellar signals due to activity or granulation negatively impact the detectability of low-mass planets. Thankfully, the variability of the BIS parameter is a useful indicator for modulated LPV and can help to distinguish between RV signals due to low-mass companions and pulsation-related “noise”. At present it is however unclear how to mitigate the impact of modulated LPV on RV measurements.

The method for measuring RV (weak lines, strong lines, Gaussian, bi-Gaussian) also impacts the resulting pulsation-averaged velocity v_r , cf. Tab. 4, limiting the ability to search for low-mass companions using inhomogeneous data sets (cf. R. I. Anderson et al submitted). The dependence on v_r on line strength exceeds the dependence on the profile fitted to the computed CCF: v_r differs by $\sim 600 \text{ m s}^{-1}$ between weak- and strong-line RVs, whereas Gaussian and bi-Gaussian RV based on the G2 mask are consistent to within a few tens of m s^{-1} . This behavior is certainly due to the stronger asymmetry of weak line CCFs (§3.2), which is more pro-

nounced near maximum than near minimum RV, thus biasing v_γ (cf. Nardetto et al. 2008). Studies aiming to investigate binarity or Galactic rotation curves (e.g. Pont et al. 1997) may thus benefit from employing strong-line RVs, since these exhibit weaker asymmetry and are thus less biased. On the other hand, studies interested in revealing modulated LPV in Cepheids may benefit from using weak-line RVs as a first indicator.

In summary, different use cases may benefit from using differently defined RVs. However, the definition of the RV measurement can lead to phase-dependent differences among RV measured using different instruments, or even by different authors. Employing consistently defined RVs is thus crucial for high-precision RV analyses, e.g. when investigating Cepheid binarity. For the time being, it is unclear whether RV curve modulation can be avoided by defining the measurement adequately. However, averaging over long temporal baselines may cancel out these effects, cf. §4.3 below.

4.3 Implications for Baade-Wesselink Distance and p -factors

RV curve modulation represents a difficulty for Baade-Wesselink type analyses that exploit Cepheid pulsations to measure quasi-geometric distances. Specifically, distance

$$d \propto \Delta R / \Delta \Theta = p / \Delta \Theta \int v_r d\phi, \quad (2)$$

where p is the projection factor required to translate the observed, disk-integrated line-of-sight velocity into the pulsational velocity, $\Delta \Theta$ is the full-amplitude angular diameter variation, and the RV integral is computed over the same phase range. $\Delta \Theta$ can be averaged over many cycles (e.g. Breifelder et al. 2016), or determined for individual half-cycles of expansion or contraction (A16). As argued in A14, cycle-to-cycle and longer-term changes in RV amplitude and shape result in systematic changes of the RV integral. This introduces a systematic distance uncertainty if the measured ΔR and $\Delta \Theta$ are not equivalent, e.g. by not being measured contemporaneously or by other systematics intervening even if measured contemporaneously.

p -factors have been decomposed as follows (Nardetto et al. 2007):

$$p = p_0 \cdot f_{\text{grad}} \cdot f_{\text{o-g}}, \quad (3)$$

where f_{grad} is a factor representing the impact of velocity gradients, $f_{\text{o-g}}$ represents the difference between the motion of optical and gas layers, and p_0 represents all other effects such as geometry and limb darkening.

A16 investigated whether angular diameter variations repeated perfectly, or whether they, too, exhibit modulated variability. They further investigated whether any modulation pattern would reproduce the trends exhibited by RV data. The high-quality interferometric dataset obtained for ℓ Car showed tentative signs of modulated angular variability, although contributions from instrumental effects could not be fully excluded. Interestingly, however, RV and angular diameters exhibited very different modulation behavior, which was interpreted as being the result of the different motions of the optical continuum (measured by interferometry) and the gas (measured via spectral lines). This can be expressed as a complex time dependence—possibly changing from cycle to cycle—not previously considered for factor $f_{\text{o-g}}$ in Eq. 3.

Section 3.3 demonstrates that ℓ Car’s velocity gradients also exhibit a complex time-dependence, which is furthermore not in phase with the pulsations and enters the definition of p via a previously unknown time-dependence of factor f_{grad} . Having measured

RV using different line masks and profiles fitted to CCFs, let us now consider the impact of how RV is defined on p .

Table 4 lists values of RV integrals, $\int v_r d\phi = \Delta R/p$, computed for RVs based on three different correlation masks, as well as bi-Gaussian RVs based on the G2 mask, measured for the individual half-cycles accessible. The duration of each half-cycle is determined as described in §2 using pulsation-averaged v_γ (cf. §4.2). $\Delta R/p$ is then computed as done previously (A14, A16) using cubic splines and Monte Carlo simulations (10 000 draws). Note that durations and $\Delta R/p$ can differ here from the values presented in A14 and A16 due to different definitions of v_γ .

The row labeled $\langle |\Delta R/p| \rangle$ in Table 4 lists average absolute values of $\Delta R/p$ depending on the definition of the RV measurement. $\langle |\Delta R/p| \rangle$ depends significantly on the method employed to measure RV (e.g. Gaussian vs. bi-Gaussian fits to CCFs), as expected from the different RV amplitudes, cf. Fig. 5. The row labeled σ lists the standard deviation of all $|\Delta R/p|$ and is followed by the fractional standard deviation, $\sigma / \langle |\Delta R/p| \rangle$, which shows that Gaussian RVs based on strong spectral lines yield the most consistent result for $\Delta R/p$, exhibiting a scatter of 2.3% compared to a scatter of 3.0% for bi-Gaussian RVs. Gaussian RVs based on the G2 mask yield the second most consistent results among pulsation cycles, with a scatter of 2.6%, followed by weak-line RVs. This behavior is directly related to the cycle-to-cycle changes in the BIS parameter, which directly affects bi-Gaussian RVs, and is expressed more strongly for weak-line CCFs, cf. §3.2.

Importantly, the definition of the RV measurement employed directly affects the value of the projection factor obtained in empirical p -factor calibrations. To illustrate this point, let us adopt ℓ Car’s distance of 497.5 pc (Benedict et al. 2007), the average $\langle \Delta \Theta \rangle = 0.569$ of two consecutive half-cycles (A16), and the average $\langle |\Delta R/p| \rangle$ to determine $p = d \cdot \Delta \Theta / (9.3095 \cdot \langle |\Delta R/p| \rangle)$, assuming $R_\odot = 696\,342$ km (Emilio et al. 2012). Statistical uncertainties are not included for this comparison whose aim is to illustrate the dependence of p on the RV measurement technique. p is thus found to range from 1.207 for bi-Gaussian RVs to 1.330 for weak-line RVs, even when averaging over many pulsation cycles. p thus implicitly depends on the definition of the RV measurement by up to 10%. This compares to the $\sim 10\%$ uncertainty on empirical p -factor calibrations imposed by the accuracy of current parallax measurements (Breifelder et al. 2016). As this comparison shows, employing a consistent definition of RV measurements is crucial for determining p -factors and in particular for calibrating a p - P_{puls} -relation (Nardetto et al. 2007; Breifelder et al. 2016).

Summing over $\Delta R/p$ of consecutive half-cycles listed in Tab. 4 reveals no significant net growth or shrinkage in linear radius (mean growth is $-0.04 R_\odot/p$ with $\sigma = 0.96 R_\odot/p$ for Gaussian RVs computed with G2 mask), i.e., short-term differences in $\Delta R/p$ cancel out over longer timescales. This suggests that a consistent value of $\Delta R/p$ can be determined if sufficiently many pulsation cycles are averaged.

5 CONCLUSIONS

This paper investigates the origin of cycle-to-cycle and longer-term modulations of long-period Cepheid RV curves as discovered recently (A14) using ℓ Carinae as an example. CCFs were computed based on 925 high-SNR high-resolution optical spectra observed during three campaigns (2014, 2015, and 2016), each of which cover at least two complete consecutive pulsation cycles. Cycle-to-cycle differences in the spectral line profile variability pattern

Cycle	N_{RV}	weak line, Gaussian $v_\gamma = 2.930 \text{ km s}^{-1}$		G2 mask, Gaussian $v_\gamma = 3.419 \text{ km s}^{-1}$		G2 mask, bi-Gaussian $v_\gamma = 3.441 \text{ km s}^{-1}$		strong lines, Gaussian $v_\gamma = 3.571 \text{ km s}^{-1}$	
		duration [d]	$\Delta R/p$ [R_\odot]	duration [d]	$\Delta R/p$ [R_\odot]	duration [d]	$\Delta R/p$ [R_\odot]	duration [d]	$\Delta R/p$ [R_\odot]
c14a	55	18.467(7)	22.135(8)	18.379(7)	22.888(7)	18.13(2)	24.47(2)	18.318(6)	23.395(8)
c14b_1	50	17.074(8)	-22.436(7)	17.174(6)	-23.185(7)	17.32(2)	-24.35(2)	17.250(6)	-23.830(7)
c14b_2	37	18.555(8)	23.489(8)	18.442(6)	24.102(8)	18.37(2)	26.10(2)	18.363(6)	24.556(8)
c14c [†]	115	16.84(6)	-22.02(1)	16.96(6)	-22.74(1)	17.3(2)	-24.16(5)	17.10(7)	-23.38(1)
c15a_1	66	16.917(1)	-22.554(2)	17.046(1)	-23.355(1)	17.269(4)	-24.950(3)	17.133(1)	-24.006(1)
c15a_2	81	18.624(1)	23.848(2)	18.500(1)	24.374(1)	18.256(4)	26.509(3)	18.417(1)	24.802(1)
c15b_1	86	17.087(2)	-22.873(2)	17.223(1)	-23.686(1)	17.328(4)	-25.182(3)	17.316(2)	-24.334(1)
c15b_2	58	18.414(2)	22.798(2)	18.280(1)	23.399(1)	18.189(4)	26.142(4)	18.188(2)	23.866(2)
c15c [†]	32	17.155(2)	-23.605(2)	17.272(2)	-24.335(1)	17.517(6)	-26.135(4)	17.347(2)	-24.938(2)
c16b_1	53	17.071(1)	-23.256(1)	17.154(1)	-23.978(1)	17.284(3)	-25.274(3)	17.214(1)	-24.580(1)
c16b_2	57	18.420(1)	22.551(2)	18.340(1)	23.430(1)	18.237(4)	24.338(3)	18.283(1)	24.151(1)
c16c_1	54	17.280(2)	-23.625(2)	17.369(1)	-24.337(1)	17.500(4)	-25.881(3)	17.436(1)	-24.931(1)
c16c_2 [‡]	19	18.277(2)	21.986(4)	18.183(1)	22.962(2)	18.043(4)	23.967(7)	18.121(2)	23.724(3)
$\langle \Delta R/p \rangle$			22.860		23.598		25.189		24.192
σ			0.648		0.580		0.885		0.545
$\sigma/\langle \Delta R/p \rangle$			0.028		0.026		0.030		0.023
p [$d = 497.5 \text{ pc}$, $\Delta\Theta = 0.56895 \text{ mas}$]			1.330		1.288		1.207		1.257

Table 4. Dependence of v_γ , half-cycle duration, integral of RV curve—here denoted by $\Delta R/p$ —, and projection factors p required for Baade-Wesselink distance measurements per pulsation half-cycle (contraction/expansion) on measurement technique and lines used to compute RV. Cycles are labeled as in Fig. 4, with .1 and .2 denoting first and second half of cycle. Statistical uncertainties are listed for duration and $\Delta R/p$ using the notation 18.467(7) = 18.467 ± 0.007 and are based on 10 000 Monte Carlo repetitions. [†] marks cycles determined by extrapolation to nearest v_γ , [‡] marks the cycle with the fewest observations, for which the spline fit is not as well constrained due to larger gaps in phase coverage. Fluctuations of the average $\Delta R/p$ per method are 2–3 percent. p -factors are computed for each method assuming distance (Benedict et al. 2007) and angular diameter variation (Anderson et al. 2016a, using the average of both measurements) as stated to illustrate systematic differences in p .

are investigated and found to be significant, even among consecutive cycles, becoming more noticeable over longer timescales. The asymmetry parameter BIS exhibits the most peculiar cycle-to-cycle variability and is considered in detail.

The dependence of the inferred RV variability on the measurement technique is investigated by computing CCFs for three different line masks (G2, weak lines, strong lines) and measuring RV by fitting either Gaussian or bi-Gaussian profiles. Bi-Gaussian RVs exhibit stronger RV curve modulation than Gaussian RVs, since the primary effect of modulated line profile variability concerns asymmetry and since bi-Gaussians are by construction sensitive to such asymmetry. Weak-line CCFs generally exhibit stronger asymmetry than strong-line CCFs and are more strongly affected by cycle-to-cycle variations.

Modulated BIS variability primarily originates in long-term (cycle-to-cycle and longer) variations of atmospheric velocity gradients and can therefore serve to identify this effect. This is important, since BIS provides a straightforward means to distinguish temporal variations in the pulsation-averaged velocity v_γ due to modulated line profile variability (modulated BIS variability) from ones caused by orbital motion (no modulated BIS variability).

Visualization of cycle-to-cycle changes in velocity gradient indicates the atmosphere to retain memory of the preceding cycle. The modulation pattern seen for BIS suggests a possible repetition of this parameter’s variability over a timescale of $\sim 2 \text{ yr}$, which is close to the expected rotation period for a star such as $\ell \text{ Car}$. Establishing a recurrence or even periodicity of this kind would be invaluable for better understanding the origin of cycle-dependent velocity gradient variations.

Possible origins of modulated line profile variations as well as their relevance for BW distances are discussed, underlining the

importance of consistently defined RV measurements for BW distances. Since RV curve modulation tends to average out over long timescales, it is advantageous for BW analyses to reduce exposure to individual pulsation cycles. This will be of particular importance when *Gaia* will soon enable the empirical calibration of projection factors for hundreds of Galactic Cepheids.

More generally, this work exposes previously unknown complexity in the pulsation of Cepheids and opens a new window to further the understanding of stellar pulsations.

ACKNOWLEDGMENTS

Useful discussions with Xavier Dumusque and the assistance of many observers are acknowledged. I am grateful to the entire Euler team, the Geneva stellar variability group, and the Geneva exoplanet group for their assistance and support. The friendly and competent assistance by all ESO and non-ESO staff at La Silla Observatory was greatly appreciated. The anonymous referee’s timely and positive response is acknowledged.

The Swiss Euler telescope is funded by the Swiss National Science Foundation. The ability to operate such long-term campaigns on a small telescope with high-quality instrumentation was crucial to this work’s ability to illustrate the complex behavior of Cepheid pulsations in this amount of detail.

This research was funded by the Swiss National Science Foundation via an Early Postdoc.Mobility fellowship and has made use of NASA’s ADS Bibliographic Services.

REFERENCES

- Alvarez R., Jorissen A., Plez B., Gillet D., Fokin A., Dedecker M., 2001, *A&A*, **379**, 288
- Anderson R. I., 2014, *A&A*, **566**, L10
- Anderson R. I., Ekström S., Georgy C., Meynet G., Mowlavi N., Eyer L., 2014, *A&A*, **564**, A100
- Anderson R. I., Sahlmann J., Holl B., Eyer L., Palaversa L., Mowlavi N., Süveges M., Roelens M., 2015, *ApJ*, **804**, 144
- Anderson R. I., et al., 2016a, *MNRAS*, **455**, 4231
- Anderson R. I., Saio H., Ekström S., Georgy C., Meynet G., 2016b, *A&A*, **591**, A8
- Baade W., 1926, *Astronomische Nachrichten*, **228**, 359
- Baranne A., et al., 1996, *A&AS*, **119**, 373
- Belopolsky A., 1894, *Astronomische Nachrichten*, **136**, 281
- Benedict G. F., et al., 2007, *AJ*, **133**, 1810
- Blažko S., 1907, *Astronomische Nachrichten*, **175**, 325
- Böhm-Vitense E., Love S. G., 1994, *ApJ*, **420**, 401
- Bowman D. M., Kurtz D. W., Breger M., Murphy S. J., Holdsworth D. L., 2016, *MNRAS*, **460**, 1970
- Breitfelder J., Mérand A., Kervella P., Gallenne A., Szabados L., Anderson R. I., Le Bouquin J.-B., 2016, *A&A*, **587**, A117
- Buchler J. R., Kolláth Z., 2001, *ApJ*, **555**, 961
- Buchler J. R., Yecko P. A., Kolláth Z., 1997, *A&A*, **326**, 669
- Burki G., Mayor M., Benz W., 1982, *A&A*, **109**, 258
- Butler R. P., 1993, *ApJ*, **415**, 323
- Dawe J. A., 1969, *MNRAS*, **145**, 377
- Derekas A., et al., 2012, *MNRAS*, **425**, 1312
- Deutsch A. J., 1958, in Lehnert B., ed., *IAU Symposium Vol. 6, Electromagnetic Phenomena in Cosmical Physics*. p. 209
- Emilio M., Kuhn J. R., Bush R. I., Scholl I. F., 2012, *ApJ*, **750**, 135
- Engle S. G., Guinan E. F., Harper G. M., Neilson H. R., Remage Evans N., 2014, *ApJ*, **794**, 80
- Evans N. R., et al., 2015a, *AJ*, **150**, 13
- Evans N. R., et al., 2015b, *MNRAS*, **446**, 4008
- Figueira P., Santos N. C., Pepe F., Lovis C., Nardetto N., 2013, *A&A*, **557**, A93
- Fokin A. B., Gillet D., Breitfellner M. G., 1996, *A&A*, **307**, 503
- Goncharskii A. V., Stepanov V. V., Kokhlova V. L., Yagola A. G., 1977, *Soviet Astronomy Letters*, **3**, 147
- Goodricke J., 1786, *Royal Society of London Philosophical Transactions Series I*, **76**, 48
- Gray D. F., Stevenson K. B., 2007, *PASP*, **119**, 398
- Gray D. F., Toner C. G., 1986, *PASP*, **98**, 499
- Grossmann-Doerth U., 1994, *A&A*, **285**, 1012
- Grunhut J. H., Wade G. A., Hanes D. A., Alecian E., 2010, *MNRAS*, **408**, 2290
- Guzik J. A., Kosak K., Bradley P. A., Jackiewicz J., 2016, preprint, ([arXiv:1605.04443](https://arxiv.org/abs/1605.04443))
- Hadrava P., Šlechta M., Škoda P., 2009, *A&A*, **507**, 397
- Karp A. H., 1973, *ApJ*, **180**, 895
- Karp A. H., 1975, *ApJ*, **201**, 641
- Karp A. H., 1978, *ApJ*, **222**, 578
- Kervella P., Coudé du Foresto V., Perrin G., Schöller M., Traub W. A., Lacasse M. G., 2001, *A&A*, **367**, 876
- Kervella P., Fouqué P., Storm J., Gieren W. P., Bersier D., Mourard D., Nardetto N., du Coudé Foresto V., 2004, *ApJ*, **604**, L113
- Kiss L. L., Vinkó J., 2000, *MNRAS*, **314**, 420
- Kolenberg K., et al., 2010, *ApJ*, **713**, L198
- Kovtyukh V. V., Andrievsky S. M., Luck R. E., Gorlova N. I., 2003, *A&A*, **401**, 661
- Kraft R. P., 1967, in Thomas R. N., ed., *IAU Symposium Vol. 28, Aerodynamic Phenomena in Stellar Atmospheres*. p. 207
- Marmier M., et al., 2013, *A&A*, **551**, A90
- Mathias P., Gillet D., Fokin A. B., Nardetto N., Kervella P., Mourard D., 2006, *A&A*, **457**, 575
- Molnár L., Szabados L., Dukes Jr. R. J., Györfy Á., Szabó R., 2013, *Astronomische Nachrichten*, **334**, 980
- Mundprecht E., Muthsam H. J., Kupka F., 2013, *MNRAS*, **435**, 3191
- Mundprecht E., Muthsam H. J., Kupka F., 2015, *MNRAS*, **449**, 2539
- Nardetto N., Mourard D., Kervella P., Mathias P., Mérand A., Bersier D., 2006, *A&A*, **453**, 309
- Nardetto N., Mourard D., Mathias P., Fokin A., Gillet D., 2007, *A&A*, **471**, 661
- Nardetto N., Stoekl A., Bersier D., Barnes T. G., 2008, *A&A*, **489**, 1255
- Neilson H. R., Ignace R., 2014, *A&A*, **563**, L4
- Neilson H. R., Engle S. G., Guinan E. F., Bisol A. C., Butterworth N., 2016, *ApJ*, **824**, 1
- Nordgren T. E., Armstrong J. T., Germain M. E., Hindsley R. B., Hajian A. R., Sudol J. J., Hummel C. A., 2000, *ApJ*, **543**, 972
- Pepe F., Mayor M., Galland F., Naef D., Queloz D., Santos N. C., Udry S., Burnet M., 2002, *A&A*, **388**, 632
- Pont F., Queloz D., Bratschi P., Mayor M., 1997, *A&A*, **318**, 416
- Poretti E., Le Borgne J. F., Rainer M., Baglin A., Benkő J. M., Debosscher J., Weiss W. W., 2015, *MNRAS*, **454**, 849
- Queloz D., et al., 2001a, *The Messenger*, **105**, 1
- Queloz D., et al., 2001b, *A&A*, **379**, 279
- Riess A. G., et al., 2016, preprint, ([arXiv:1604.01424](https://arxiv.org/abs/1604.01424))
- Sanford R. F., 1956, *ApJ*, **123**, 201
- Sasselov D. D., Lester J. B., 1990, *ApJ*, **362**, 333
- Sasselov D. D., Fieldus M. S., Lester J. B., 1989, *ApJ*, **337**, L29
- Schmidt E. G., Parsons S. B., 1984, *ApJ*, **279**, 202
- Schwarzschild M., 1952, in Oosterhoff P. T., ed., *Vol. VIII, Transactions of the IAU*. Cambridge University Press, p. 811
- Ségransan D., et al., 2010, *A&A*, **511**, A45
- Soszyński I., et al., 2008, *Acta Astron.*, **58**, 163
- Soszyński I., et al., 2015a, *Acta Astron.*, **65**, 297
- Soszyński I., et al., 2015b, *Acta Astron.*, **65**, 329
- Stothers R. B., 2009, *ApJ*, **696**, L37
- Szabó R., et al., 2010, *MNRAS*, **409**, 1244
- Toner C. G., Gray D. F., 1988, *ApJ*, **334**, 1008
- Wallerstein G., Jacobsen T. S., Cottrell P. L., Clark M., Albrow M., 1992, *MNRAS*, **259**, 474
- Wallerstein G., Albright M. B., Ritchey A. M., 2015, *PASP*, **127**, 503
- Wesselink A. J., 1946, *Bull. Astron. Inst. Netherlands*, **10**, 91